Multidecade Global Flux Datasets from the Objectively Analyzed Air-sea Fluxes (OAFlux) Project: Latent and Sensible Heat Fluxes, Ocean Evaporation, and Related Surface Meteorological Variables

Lisan Yu

Xiangze Jin

Robert A. Weller

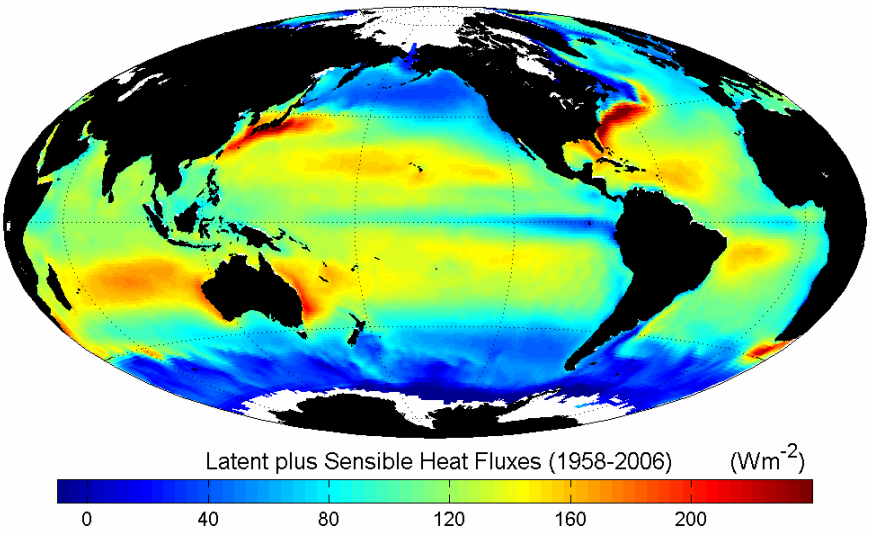

Woods Hole Oceanographic Institution

OAFlux Project Technical Report (OA-2008-01)

January 2008

Abstract

This report supports the release of the third version of global ocean-surface heat flux products (1958-2006) developed by the Objectively Analyzed air-sea Heat Fluxes (OAFlux) project. The OAFlux products are constructed not from a single data source, but from an optimal blending of satellite retrievals and three atmospheric reanalyses. Daily fluxes are computed from the optimally estimated variables using the COARE bulk flux algorithm 3.0.

This report documents the methodology, strategy, and procedure used in developing the 49-year (1958-2006) analysis of global latent, sensible heat fluxes, and ocean evaporation. Error estimates for flux and related variable fields are provided. The report includes the comparisons with two ship-based climatologies, three model reanalyzed fluxes, and 107 in situ flux time series. OAFlux estimates are unbiased and have the smallest mean error: the mean OAFlux-buoy difference is of 1.0 Wm^{-2} and the mean difference in absolute measure is of 7.4 Wm^{-2}.

Monthly products are made for the entire 49-year period, and daily products are available from 1985 onward. The datasets are freely available to interested users for non-commercial scientific research. For further information, please visit the project website at http://oaflux.whoi.edu/. The project is sponsored by the NOAA Office of Climate Observation.

3 key words: atmosphere-ocean interactions**,** sea surface heat exchange, ocean evaporation

TABLE OF CONTENTS

1. Introduction

This report supports the release of the third version of global ocean-surface heat flux products (1958-2006) developed by the Objectively Analyzed air-sea Heat Fluxes (OAFlux) project at the Woods Hole Oceanographic Institution (WHOI). The first version was made for the Atlantic Ocean (1988-1999) and released in March 2004. The second version was for the global oceans (1981-2002) and released in December 2005. This third version consists of a 49-year analysis of latent and sensible heat fluxes, ocean evaporation, and flux-related surface meteorological variables on daily and 1-degree resolution.

Latent and sensible heat flux estimates are commonly computed from the parameterization of the fluxes as a function of surface meteorological observables, such as wind speed, sea-air humidity and temperature gradients, etc (Liu et al., 1979). These flux-related variables are obtainable from three major sources: marine surface weather reports from Voluntary Observing Ships (VOS), satellite remote sensing, and NWP reanalysis and operational analysis outputs. Correspondingly, the heat flux products are grouped into three categories: ship based products, satellite-based products, and NWP reanalysis products. Ship-based products have long been used to determine the climatology of global air-sea exchanges (Bunker, 1976; Esbensen and Kushnir, 1981; Isemer and Hasse, 1985, 1987; Hsiung, 1985; Oberhuber, 1988; Cayan, 1992a,b,c, da Silva et al., 1994; Josey et al., 1998). Satellite based products have advanced the near real-time capability for estimating space-time variability of air-sea fluxes with unprecedented resolution and coverage (Chou et al., 1995; Schulz et al., 1997; Curry et al., 1999; Kubota et al. 2002; Bentamy et al. 2003). NWP model outputs from such centers as the National Centers for Environmental Prediction (NCEP; Kalnay et al. 1996; Kanamitsu et al. 2002) and European Centre for Medium-Range Weather Forecasts (ECMWF; Uppala et al. 2005) have provided real-time simulation of global heat fluxes and variability with uniform spatial and temporal resolutions since the 1950s. Integrally, the three types of heat flux products have contributed significantly to our understanding of the global energy budget in general and of the role of the ocean in modulating climate through feedback processes in particular.

Different data sources have different advantages and disadvantages. Ship-based observations have good accuracy and long time series but poor global coverage, as observations are concentrated along ship routes. Satellite retrievals have good accuracy and excellent global coverage but shorter data record. NWP fluxes have good global coverage and long time series

but suffer from model biases. However, by using an advanced objective analysis, the OAFlux project demonstrated that the advantages of existing data sources can be combined to produce a synthesized flux time series with improved accuracy. The term, objective analysis, originally denotes the process of combining data that are generally non-uniformly distributed and have errors associated with them. The process involves searching for a solution that has a minimum error variance (Daley, 1991). Objective analysis has received wide applications after its first introduction to NWP by Panofsky (1949), and now covers a broad range of techniques. Some ship-based flux climatological analyses (da Silva et al. 1994; Josey et al. 1999) used a simple iterative difference-correction scheme based on the method of successive corrections (Bergthorsson and Döös 1955). Modern objective analysis techniques, such as statistical interpolation and variational analysis, have been applied to such products as sea surface temperature (SST) (Reynolds et al. 2002), precipitation (Xie and Arkin 1996), pseudostress (Legler et al. 1989), and surface wind (Atlas et al. 1996).

Thus, the OAFlux products are constructed not from a single data source, but from an optimal blending of satellite retrievals and three atmospheric reanalyses. The OAFlux project improves the estimates of latent and sensible heat fluxes through utilizing the best possible surface meteorological variables and the best possible bulk algorithm. At present, the bulk algorithm 3.0 (Fairall et al, 1996a,b; 2003; Bradley et al., 2000) developed from the field experiments of the Tropical Ocean Global Atmosphere Coupled Ocean-Atmosphere Response Experiment (TOGA COARE) (Webster and Lukas, 1992) represents the state-of-art flux parameterization. The best possible estimates for those surface meteorological variables are obtained through applying a variational approach that seeks optimal synthesis of satellite and NWP data sources. The variational approach for improving flux-related variables was initially developed and implemented by Yu et al. (2004a,b; 2006) for the Atlantic Ocean fluxes during the period 1988–1999, and was later extended to the Indian Ocean (Yu et al. 2007), and global ocean basins for the period from 1981 to 2005 (Yu and Weller 2007).

This report documents the methodology, strategy, and procedure used in developing the 49-year (1958-2006) analysis of global latent and sensible heat fluxes. The report is organized as follows. Section 2 gives a brief description of the COARE bulk algorithm 3.0, required basic variable inputs, and the input data sources. Section 3 describes the methodology of synthesis and the strategy used in the OAFlux synthesis. Section 4 characterizes the 49-year mean fields of

latent and sensible heat fluxes as well as basic variables produced by OAFlux. Section 5 compares the 49-year mean OAFlux fields with two ship-based climatologies and the long-term means of three NWP reanalyzed fluxes. Section 6 presents the validation analysis of using 107 (105 buoys plus 2 ships) in situ flux measurements to evaluate the OAFlux estimates along with three NWP fluxes. Section 7 provides basin-wide error estimates for OAFlux variable and flux fields. Summary is given in section 8.

2. COARE bulk flux algorithm and input data sources for synthesis

2.1 COARE bulk algorithm 3.0

Bulk aerodynamic formulae are derived from the Monin-Obukhov similarity approach (Liu et al., 1979). The formulae relate turbulent fluxes to mean values of surface meteorological variables such as surface temperature, wind, and surface air temperature and humidity. The bulk expressions of the respective latent and sensible heat fluxes, Q_{LH} and Q_{SH}, are

$$Q_{LH} = \rho\, L_e\, c_e\, U\, (q_s - q_a) \qquad (1)$$

$$Q_{SH} = \rho\, c_p\, c_h\, U\, (T_a - \theta) \qquad (2)$$

where ρ is the density of air, L_e the latent heat of evaporation, c_p the specific heat capacity of air at constant pressure, and U the wind speed relative to the sea surface at the height of z_r. The turbulent exchange coefficients for latent and sensible heat fluxes are denoted by c_e and c_h respectively, and are function of wind speed, height, and atmospheric stability. The surface and near-surface atmospheric specific humidities are denoted by q_s and q_a, respectively, while the sea surface skin temperature is represented by T_s and the near surface air potential temperature by θ. Note that q_s is computed from the saturation humidity, q_{sat}, for pure water at T_s,

$$q_s = 0.98\, q_{sat}\, (T_s) \qquad (3)$$

where a multiplier factor of 0.98 is used to take into account the reduction in vapor pressure caused by a typical salinity of 34 psu. In addition, θ includes a correction for the adiabatic lapse rate, γ,

$$\theta = T_a + \gamma z_r \qquad (4)$$

where T_a is the air temperature at z_r.

There are several forms of bulk flux algorithms currently available (Brunke et al. 2002). The differences between the algorithms reside in the differences in treating the parameterizations of the transfer coefficients c_e and c_h, conditions of light wind and stable stratification, influence of sea spray, treatment of sea state (swell, directional effects), appropriate averaging scales, parameterization of mesoscale gustiness, and the behavior of scalar sublayer transfer. The OAFlux project uses state-of-the-art COARE bulk flux algorithm version 3.0 to compute the fluxes.

The COARE bulk flux algorithm has evolved over several development phases. The algorithm was initially developed from the model of Liu-Katsaros-Businger (LKB; Liu et al., 1979) for use by the COARE research community under the light wind (0–12 ms^{-1}), strongly convective conditions over the western Pacific warm pool region (Fairall et al. 1996b). Since then, efforts have continually been made toward the application of the algorithm outside the tropical oceans in conditions of midlatitudes, colder waters, and higher wind speeds (Bradley et al. 2000; Fairall et al. 2003). This led to the updated COARE algorithm version 3.0 (Fairall et al. 2003) that has several noted improvements. The range of wind speed validity is now extended to 0–20 ms^{-1} after modifying roughness representation. The transfer coefficients are redefined in terms of conservative quantity (mixing ratio) rather than the measured quantity (water vapor density), thus eliminating the need for a Webb et al. (1980) correction to latent heat flux. The mean profile stability functions are adjusted and the number of iterations to solve for stability has been shortened considerably. The COARE 3.0 is shown to be accurate within 5% for wind speeds of 0–10 m s^{-1} and 10% for wind speeds between 10 and 20 m s^{-1}. The major remaining issues for the algorithm are the influence of surface waves on the fluxes and the quantification of the effects of sea spray droplets at winds exceeding 15-20 ms^{-1}.

2.2 Required basic variable inputs

In Eqs. (1)–(4), only U, T_s, T_a and q_a are independent. In other words, once the information of theses four variables are given, all the other variables, including the transfer coefficients, can be determined from respective parameterizations. The OAFlux project provides the best estimates for these four variables by using an advanced objective analysis. As described

in Section 2.3, the study uses U at 10 m, T_a and q_a at 2 m, T_s at the sea surface to be consistent with the reference levels used in the NWP models.

2.3 Input data sources

The OAFlux project targets on daily and 1°×1° resolution for the global ocean basins that are free from ice. To obtain the best possible global daily estimates for U, T_s, T_a and q_a, the OAFlux synthesis uses surface meteorological fields derived from satellite remote sensing and reanalysis outputs produced from NCEP and ECMWF models. Satellite sensors, though offering accurate observations for near surface wind U and sea surface temperature T_s, have technical difficulties in retrieving air temperature and humidity at a few meters above the sea surface. In addition, satellite observations do not offer 100% global coverage on daily basis. Hence, the inclusion of NWP model outputs is intended for two purposes: to fill in the data information that satellites are unable to provide and to fill in the gaps that are missed between swaths. The OAFlux synthesis does not assimilate ship meteorological reports, such as the database of the Comprehensive Ocean-Atmosphere Data Set (COADS) project. The main reason is that the coverage of ship routes on a daily basis is extremely sparse compared to the global coverage of satellite retrievals and NWP model outputs. The inadequate daily coverage limits the influence of ship measurements on the global synthesis. However, given that ship observations have a time series of multiple decades and are a reliable source for climatological flux atlases, the OAFlux project uses ship-based observations to identify biases in NWP model variables and to choose the weights for synthesis (Section 3). The OAFlux project also uses the ship-based flux atlas as an independent verification for the mean flux patterns computed by OAFlux (Section 6).

2.3.1 Satellite observations

Satellite products in the OAFlux synthesis include wind speed retrievals from both active (scatterometer) and passive (radiometer) microwave remote sensing, and SST daily high-resolution blended analysis by Reynolds et al. (2007). The synthesis includes also the near-surface humidity product that was derived by Chou et al. (2001) from Special Sensor Microwave Imager (SSM/I) column water vapor retrievals. A brief description of each of the satellite data sources is given below.

a. Wind speed

There are three input data sources of satellite wind speeds: two from passive radiometers SSMI and AMSR-E (Advanced Microwave Scanning Radiometer – Earth Observing System), and one from the QuikSCAT scatterometer.

SSMI has been operating since July 1987 on board a series of Defense Meteorological Satellite Program (DMSP) spacecraft in a circular sun-synchronous near-polar orbit at an altitude of approximately 860 km and orbit period of 102 min. The 1394-km swath of the SSMI covers 82% of the earth surface between 87°36′S and 87°36′N in 24 hours, and produces a complete coverage within three days (Wentz, 1997). SSM/I is a seven channel passive microwave radiometer operating at four frequencies (19.35, 22.235, 37.0, and 85.5 GHz) and dual-polarization (except at 22.235 GHz which is V-polarization only). The Wentz (1997) algorithm relates wind speed both to the brightness temperatures computed from the 37 GHz horizontal and vertical polarized radiance measurements and to the radiative transfer and absorption between the sea surface and satellite. The data are available at a resolution of 12 hourly and at a swath resolution of 25 km. Wind speeds are flagged if cloud/rain liquid water values exceeding 18 mg cm^{-2} because the accuracy of the wind speed retrievals quickly degrades in the presence of rain. Wind speed values are also flagged if the measurements are within 50-100 km of the coast or within 200 km of the climatological-mean monthly position of the ice edge. The wind speeds have a root-mean-square (RMS) difference of 1.6 m s^{-1} and zero bias as compared to buoy measurements (Wentz, 1997).

AMSR-E was developed by the National Space Development Agency of Japan (NASDA) and was launched on the NASA's Aqua satellite on May 4, 2002 in a sun synchronous near-polar low orbit at an altitude of 705 km and period of 99 min. AMSR-E scans conically across a 1445-km swath and makes dual-polarized passive microwave measurements at six frequencies: 6.925, 10.65, 18.7, 23.8, 36.5, and 89.0 GHz. Vertically and horizontally polarized measurements are taken at all channels. AMSR-E was built upon the heritage of the SSM/I and Microwave Imager for the Tropical Rain Measuring Mission (TRMM TMI). Because of the more low-frequency measurement channels and improved spatial resolution at higher frequency channels, AMSR-E represents an improvement over SSM/I. AMSR-E is also an advancement from TMI. The latter has a 10.65 GHz channel, but its unique equatorial orbit mainly covers the Tropics (from about

38°S to 38°N) unlike the global coverage of AMSR-E. Comparison of the AMSR-E wind speed with collocated wind speeds from TMI and three SSM/Is shows an rms difference of 0.51 ms^{-1} over the 3-month period from June through August 2002. A daily-mean comparison between AMSR-E and buoy measurements produces an rms of 0.6 ms^{-1} or less across all buoy locations.

The NASA QuikSCAT was launched into a sun-synchronous near polar orbit on June 19, 1999, at an altitude of approximately 800 km and period of 101 min. The main instrument on the QuikSCAT satellite is SeaWinds, which is an active radar scatterometer. This scatterometer operates by transmitting microwave pulses at a frequency of 13.4 GHz (Ku-band) to the ocean surface and measuring the echoed radar pulses bounced back to the satellite. Wind speed and direction at 10 m above the surface of the water are then derived from the backscatter energy. The instrument has unprecedented large swath width of 1800 km, covering 93% of the global oceans in one day. Ebuchi et al. (2002) evaluated QuikSCAT winds with wind observations from NDBC (National Data Buoy Center), TAO (Tropical Atmosphere and Ocean)/TRITON (Triangle Trans-Ocean buoy Network), and JMA (Japan Meteorological Agency) buoys. They concluded that the typical rms differences of the wind speed and direction are 1 m/s and 20 deg, respectively.

The three wind speed datasets are obtained from the Remote Sensing System website at http://www.ssmi.com/. We use SSM/I version 6, AMSR-E version 5, and QuikSCAT version 3. These winds are equivalent neutral winds referenced to a height at 10m. Equivalent neutral wind speed is the mean wind speed that would be observed if there was neutral atmospheric stratification. The wind data are available as twice daily gridded averages on a 0.25-degree grid, and are averaged onto daily and 1-degree grid resolutions of OAFlux.

b. Near surface humidity

While retrieving air humidity at a few meters above the sea surface remains difficult, the precipitable water over the oceans is readily retrievable from satellite measurements. Precipitable water is the total atmospheric water vapor contained in a vertical column of unit cross-sectional area extending from the surface to the top of the atmosphere. Experiments have been conducted using the precipitable water information to deduce the near-surface humidity. For example, Schulz et al. (1993) obtained the precipitable water in the lower 500 m of the atmospheric planetary boundary layer computed from the brightness temperatures from the 19 GHz horizontal

and 19, 22, and 37 GHz vertical polarizations. Chou et al. (1995; 1997) devised a technique for deducing daily near surface specific humidity using empirical orthogonal functions (EOF) method. This method has six categories of vertical EOFs based on total precipitable water from SSM/I and field humidity soundings over the global oceans. The resulting surface humidity at 10 m has an rms difference of 1.83 g kg^{-1} when compared to radiosonde measurements. Chou et al. (2001) released 1-degree gridded daily 10m air humidity products (1988-2000) in Version 2 of the Goddard Satellite-Based Surface Turbulent Fluxes (GSSTF) data, available from the NASA Goddard Earth Sciences Data and Information Services Center at http://disc.sci.gsfc.nasa.gov/. The SSMI 10-m humidity is height-adjusted to the 2-m humidity based on the COARE3.0 flux algorithm before being assimilated in the OAFlux synthesis.

c. SST

SST input data set is the NOAA Optimum Interpolation (OI) 0.25-degree daily SST analysis produced by Reynolds et al. (2007). The analysis has two products: one uses Advanced Very High Resolution Radiometer (AVHRR) infrared (IR) satellite SST data and the other combines AVHRR infrared with AMSR-E microwave SST data. Both products also use in situ data from ships and buoys and include a large-scale adjustment of satellite biases with respect to the in situ data. AMSR+AVHRR product begins with the start of AMSR-E data in June 2002, and it differs from the AVHRR only product because of an increase in signal variance due to the microwave sensor's near all-weather measurement capability. We opt to use the AVHRR only product for the consistency of the time series.

AVHRR is a five-channel scanner that has been flown on board the National Oceanic and Atmospheric Administration (NOAA) series of Polar Orbiting environmental Satellites (POES) in sun-synchronous orbits since November 1981. AVHRR represents the longest global record of IR SST retrievals. However, the biggest challenge in retrieving SST from an IR instrument is the cloud detection problem; because clouds are opaque to infrared radiation and can effectively mask radiation from the ocean surface. The OI daily SST analysis uses the AVHRR from the Pathfinder reanalysis project that began in January 1985. Pathfinder did not process data between November 1981 and January 1985 (during NOAA-7 flying period) because buoy data, which are used to tune the algorithm, were sparse during this period. Pathfinder data are better than the operational product, because a reanalysis allows corrections to the AVHRR dataset in a delayed

mode. The OI daily SST analysis is downloaded from the NOAA National Climate Data Center at ftp://eclipse.ncdc.noaa.gov/pub/OI-daily/NetCDF/. The 0.25-degree gridded dataset is averaged onto the 1-degree OAFlux grid.

In recent years, several high-resolution satellite microwave SST products were made available thanks to the microwave remote sensing technology that can measure SST under all weather conditions except rain. However, the microwave SST is presently not included due to two main concerns. One is that the mean of microwave SST is different from AVHRR SST because (1) microwave can penetrate clouds and thus provides a much denser coverage and also (2) the accuracy of microwave SST is slightly less than AVHRR SST. If included, the mean differences between the two sets of satellite SST products need to be resolved. The other concern, which is more decisive, is that NWP take Reynolds' AVHRR-based weekly SST products as lower boundary conditions and thus, the near-surface air temperature from the NWP models has good consistency with the AVHRR-based SST. Although SST daily variability and spatial variability could be improved for the recent few years that microwave SST is available, it may not improve the flux estimation because of the likely adversary effect on the consistency between air and sea temperatures in the NWP models.

2.3.2 NWP model reanalyses

All flux-related surface meteorological variables are readily available as gridded products every six hours from model reanalyses. The OAFlux synthesis uses the reanalyses products from two major NWP centers, namely, National Centers for Environmental Prediction (NCEP) and European Centre for Medium-Range Weather Forecasts (ECMWF).

a. NCEP1 and NCEP2

There are two versions of NCEP reanalyses. NCEP1 denotes the NCEP/NCAR reanalysis project that has produced an ongoing data set from 1948 to the present (Kalnay et al., 1996), while NCEP2 is the NCEP/DOE reanalysis project that attempts to correct known errors in NCEP1 from 1979 to present and to improve parameterizations of some physical processes (Kanamitsu et al., 2002). The two reanalysis systems use the same T62 L28 resolution, the same raw observed data, and the same turbulent flux algorithm but differ largely in the

parameterization of shortwave radiation, cloud and soil moisture. NCEP2 is regarded as an update of NCEP1 and not a next-generation reanalysis. Our previous study (Sun et al., 2002) compared the turbulent fluxes and flux-related variables from NWP models with moored buoys in the Atlantic Ocean and found that NCEP2 is less biased in the 2-m air temperature, humidity, and 10-m wind speed. However, the NCEP2 time series began after 1979. To produce the OAFlux time series prior to 1979, NCEP1 needs to be included.

NCEP1 and NCEP2 Reanalysis data are provided by the NOAA/OAR/ESRL Physical Science Division, Boulder, Colorado, USA, from their Web site at http://www.cdc.noaa.gov/. The NCEP basic variables are available every six hours, on Gaussian 192×94 grid (approximately 1.875° in longitude and latitude). The variable fields are daily averaged and interpolated linearly onto the spatial 1-degree OAFlux grid. The NCEP winds at 10m are also adjusted to the equivalent neutral wind at 10m using the COARE3.0 algorithm to make the wind compatible to the satellite wind retrievals.

b. ERA40

The ECMWF ReAnalysis–40 (ERA–40) is a global reanalysis describing the state of the atmospheric conditions during the 45 years from September 1957 to August 2002 (Uppala et al., 2005). Analyses were produced daily at 00Z, 06Z, 12Z and 18Z. The atmospheric model was run with 60 levels in the vertical, T159 spherical-harmonic representation for basic dynamic fields, and a reduced Gaussian grid with approximately uniform 125km (~1.125-degree) spacing for surface and other grid point fields.

ERA40 surface dataset is obtained from Computational Information and Systems Laboratory (CISL) at NCAR from their website at http://dss.ucar.edu/pub/era40/. Like the NCEP datasets, the ERA40 variable fields are daily averaged and interpolated linearly onto the spatial 1-degree OAFlux grid. The winds at 10m are also adjusted to the equivalent neutral wind at 10m using the COARE3.0 algorithm to make the model wind conceptually consistent with the satellite wind retrievals.

2.4 Input data for the years before and after 1985

The input data sources for each of the flux-related variables, U, T_s, q_a, and T_a are listed in Table 1. Satellite SST data started to come in January 1985. Satellite wind retrievals are available from July 1987 onward. Satellite air humidity derived from SSM/I covers the period between July 1987 and December 2000. Before 1985, NWP reanalyses are the only source of global information, with NCEP1 time series going back to 1948 and ERA40 time series back to September 1958.

The OAFlux synthesis produces optimal estimates for flux-related variables (U, T_s, q_a, and T_a) using an objective analysis. The synthesis is conducted for each day starting from September 1958 onward, during which there are at least two data sources available for each day. The quality of synthesis depends on the quality of input data sources. We are aware of the effects of NWP model biases on reanalysis outputs, and rely on satellite data, whenever available, to offset likely biases in NWP reanalyses. We are, however, aware of the difficulty of correcting NWP biases for the pre-satellite era (before 1985 in this case) due to the lack of observations. In light of satellite data availability, we divided the OAFlux analysis into two periods: before and after 1985. The two periods determined the temporal resolution of the OAFlux deliverables. Both daily and monthly products are released for the years from 1985 onward, while only monthly products are made public for the years before 1985.

3. Synthesis approach

3.1 Methodology

Through combining satellite retrievals, NCEP1&2 and ERA40 reanalyses of flux-related variables, the synthesis aims at obtaining an optimal analysis field that is as close as possible to the true state in an rms sense (i.e. it is a minimum variance estimate). The methodology governing the synthesis is based on the Gauss – Markov theorem, a standard statistical estimation theory (Daley, 1991) that has been widely used in meteorology and oceanography (e.g., Bretherton et al., 1976). This theorem states that, when combining data in a linear fashion, the linear least squares estimator is the most efficient estimator and the solution has the minimum variance. The objective analysis for ocean surface heat fluxes was first developed for the Atlantic Ocean (Yu et al. 2004a), and later was extended to global ocean basins for the period

of 1981-2005 (Yu and Weller 2007). Since them, the technique has been further refined for the OAFlux global synthesis that include both pre-satellite and satellite periods.

In essence, the application of the objective analysis involves finding a minimum of an objective function that measures the lack of fit to a set of constraints. The objective function formulated for the problem in the present study takes the form

$$
\begin{aligned}
J = {} & (X_e - FX_{ana})^T R_e (X_e - FX_{ana}) && \text{------ term (i)} \\
& + (X_{n1} - FX_{ana})^T R_{n1} (X_{n1} - FX_{ana}) && \text{------ term (ii)} \\
& + (X_{n2} - FX_{ana})^T R_{n2} (X_{n2} - FX_{ana}) && \text{------ term (iii)} \\
& + (X_s - FX_{ana})^T R_s (X_s - FX_{ana}) && \text{------ term (iv)} \\
& + \mu \left(\Delta X_{ana} / \Delta t \right)^2 && \text{------ term (v)}
\end{aligned}
\qquad (5)
$$

where the first four terms (i)–(iv) in (5) are data constraints that represent least square fitting of the analysis vector field (X_{ana}) to the estimates of ERA40 (X_e), NCEP1 (X_{n1}), NCEP2 (X_{n2}), and satellites (X_s).The superscript "T" denotes transpose. F is a linear transformation function that maps the analysis field onto data positions, and R_e, R_{n1}, R_{n2}, and R_s are the weighting matrices and inversely proportional to the error covariances of the input data X_e, X_{n1}, X_{n2}, and X_s, respectively. The fifth term is a weak constraint that ensures continuity between two consecutive daily fields, with Δt being the time interval of one day and μ a scaling parameter.

A conjugate-gradient method is used iteratively to find an optimal solution of the objective function J (Yu and O'Brien, 1991; 1995). There are total 22 global data sets being combined over the entire synthesis period (Table 1). The synthesis is processed for each of the four variables (U, T_s, q_a, and T_a) on daily basis.

3.2 Weight estimation

Error information in each input data field is needed to compute the error covariance matrix and determine the weight of each data constraint defined in (5). As the weights are inversely proportional to the error covariance matrices, the contribution of the input data to the analysis field is small if the errors are large and vice versa. So the errors of the input data determine the goodness of the fit between the analysis fields and the input data fields.

Error estimation requires basin-wide, high-accuracy observations as a reference. Such dataset is, however, severely lacking. In this study, we implemented a two-step procedure that was developed during our analysis of the ocean heat fluxes in the Atlantic Ocean (Yu et al. 2004a). The first step is to estimate the spatial structure of input data errors using COADS-based climatological atlas, and the second is step to determine the magnitude of the errors using high-quality in situ buoy measurements at available locations.

To estimate the spatial structure of the input data errors, we first express the input data (X_e, X_{n1}, X_{n2}, and X_s) in terms of a sum of the true signal (S) and their respective errors,

$$X_e = S + \varepsilon_e \qquad (6)$$

$$X_{n1} = S + \varepsilon_{n1} \qquad (7)$$

$$X_{n2} = S + \varepsilon_{n2} \qquad (8)$$

$$X_s = S + \varepsilon_s \qquad (9)$$

where ε_e, ε_{n1}, ε_{n2}, ε_s denotes the errors of the input data X_e, X_{n1}, X_{n2}, and X_s, respectively. To obtain an estimate for S, the global air-sea heat flux and surface meteorology analysis of National Oceanography Centre (NOC) (Josey et al., 1998) was used as a reference. The monthly NOC atlas was generated from the COADS database from the base period 1980–2005. The analysis included a correction of systematic errors due to variations in the measurement instruments from each individual ship meteorological report. Both validation studies with buoy measurements (Josey, 2001; Sun et al., 2003) and regional heat budget analysis (Toole et al. 2004) showed that the NOC surface meteorology and air-sea heat fluxes are at present the best in situ flux climatology.

The NOC data (X_o) can also be separated into two parts, i.e., the true signal (S) and an error (ε_o),

$$X_o = S + \varepsilon_o \qquad (10)$$

Using S in Eq.(10) to replace the S in Eqs. (6) – (9) yields,

$$X_e - X_o = \varepsilon_o + \varepsilon_e \qquad (11)$$

$$X_{n1} - X_o = \varepsilon_o + \varepsilon_{n1} \qquad (12)$$

$$X_{n2} - X_o = \varepsilon_o + \varepsilon_{n2} \qquad (13)$$

$$X_s - X_o = \varepsilon_o + \varepsilon_s \qquad (14)$$

Assuming that the errors are independent of each other, the expected covariances of the Eqs. (11) – (14) can be written as,

$$\left\langle (X_e - X_o)(X_e - X_o)^T \right\rangle = R_o + R_e \qquad (15)$$

$$\left\langle (X_{n1} - X_o)(X_{n1} - X_o)^T \right\rangle = R_o + R_{n1} \qquad (16)$$

$$\left\langle (X_{n2} - X_o)(X_{n2} - X_o)^T \right\rangle = R_o + R_{n2} \qquad (17)$$

$$\left\langle (X_s - X_o)(X_s - X_o)^T \right\rangle = R_o + R_s \qquad (18)$$

where brackets $\langle ... \rangle$ denote statistical expectations and R_o is the error covariance of the NOC data. Although Eqs. (15)–(18) provides a way to estimate the error covariances, the four equations have five unknowns (R_o, R_e, R_{n1}, R_{n2}, and R_s). To make the equations solvable, two assumptions were made. First, all the covariances in (5) are time invariant and uncorrelated in space. This assumption is commonly used in most practical applications (e.g., Legler et al., 1989; Atlas et al., 1993), as it reduces the number of high-accuracy verification data required by solving Eqs. (15)–(18). Second, NOC data errors are the sum of the errors resulting from instrumental measurements and/or from averaging/smoothing processes during the analysis, while NWP data errors come from inadequate subgrid parameterizations and model internal biases. On the climatological mean basis, NWP model errors are usually several times larger than NOC data errors. It is, therefore, reasonable to assume that R_o is small compared to the other R's and is negligible. Upon such simplifications, error variances of the input data fields can be derived from the left-hand-side of Eqs.(15)–(18).

The NOC climatological atlas, however, does not represent the "truth", though it serves as a good reference. To better quantify the error, the magnitude of the mapped error fields is further adjusted with high-accuracy observations from surface meteorological buoy measurements. Most of these buoy measurements are obtained from the Woods Hole Oceanographic Institution (WHOI) Improved METeorological instruments (IMET) (Moyer and Weller, 1997) at various sites, the TAO/TRITON buoy array in the tropical Pacific (McPhaden et al. 1998) and Indian Oceans (McPhaden et al. 2006), and the Pilot Research Moored Array in the Tropical Atlantic (PIRATA) (Servain et al. 1998). These measurements are used as benchmark time series for quantifying the effects of the neglected R_o in Eqs. (15) – (18). This is made by

tuning the amplitudes of the constructed error variances before employing them in (5). We wrote the weighting matrices R's in (5) as

$$R = \alpha \overline{R} \qquad (19)$$

where α's are to-be-determined scalars, and $\overline{R}$'s are the inversion of the time-invariant error variances estimated from the NOC data set. The α's are determined in a way that the left-hand-side of Eq. (19) agrees with the mean averages of the inversion of the error variances at all buoy sites. The amplitudes for all the weighting matrices are listed in Table 2. In general, the satellite data are assigned with larger amplitudes because their standard deviations from the buoy data are smaller; and hence, the satellite data have larger contributions to the solution in (5).

The resultant estimates of the weighting matrices should be regarded as a zero-order error approximation, due to the simplifications made in estimating the error covariances. We have assumed that the error covariances are time invariant and uncorrelated with themselves and with each other. We have used the NOC analysis as a reference data set to construct the error structures and tuned the amplitude of the error variances based on surface meteorology buoys.

Yu et al. (2004a) conducted sensitivity experiments for the Atlantic analysis to assess the sensitivity of the variable estimates to the weight selection and its effect on flux estimates. They used an experiment of constant weights to compare with the experiment that implemented the spatially varying weights from Eqs.(15)–(19). The key result they obtained is that the variable estimates are sensitive to weights in regions where input data sources have large uncertainties; one such region is the southern high latitudes. The variable estimates are less dependent of weights in regions where input data sets have better accuracy. It is apparent that the quality of input data sets is key for the optimization.

All input data sets were evaluated before being synthesized. The evaluation included comparisons with in situ buoy measurements, comparisons with NOC climatological atlas, and comparisons between satellite and NWP reanalyses. The evaluation identifies error characteristics of input datasets and uses the information to adjust the weight assignments.

4. Long-term mean fields

4.1 Latent and sensible heat fluxes

The monthly means of latent heat flux (Q_{LH}), sensible heat flux (Q_{SH}), and the sum of the two heat fluxes (Q_{LH}+ Q_{SH}) for January, July, and the annual average are shown in Figs.1-3, respectively. These monthly mean fields are constructed over the 49-year (1958-2006) analysis period. Positive fluxes indicate heat release from the ocean while negative fluxes indicate heat gain by the ocean.

The seasonal variations of Q_{LH} in the northern hemisphere are largest over the two western boundary current (WBC) regions, i.e., the Gulf Stream off the United States, and the Kuroshio and its Extension off Japan. At these places, the maximum magnitude of Q_{LH} exceeds 300 Wm^{-2} in January but reduces to less than 80Wm^{-2} in July. Like the northern hemisphere, large seasonal changes in the southern hemisphere tend to occur over such boundary current regions as the Agulhas Current off the African coast, the Falkland/Brazilian Current off South America, the eastern Australian Current, and the Leeuwin current off the west coast of Australia. Except for the last one, the other three are all western boundary currents. Yet, the flux intensification over these boundary current regions during the southern hemispheric wintertime is not as strong as their northern hemispheric counterparts. This is largely due to the fact that the continental landmasses of the Southern Ocean not only terminate in the subtropics but also are relatively narrow, and so the air masses advected over the currents are less cold and dry.

The annual mean pattern of Q_{LH} reflects the dominant wintertime features of the two hemispheres. The largest Q_{LH} magnitudes (~ 200 Wm^{-2}) are associated with the Gulf Stream and the Kuroshio and Extensions, while the second largest magnitudes (~ 150 Wm^{-2}) are located over the broad subtropical southern Indian Ocean and the boundary regions associated with the Agulhas and the Eastern Australian currents. Q_{LH} is relatively weak over the eastern Pacific and Atlantic cold tongues and also at high northern and southern latitudes. Compared to Q_{LH}, Q_{SH} is generally weak. The magnitude of Q_{SH} over the open oceans is between –5 and 15 Wm^{-2}, which is about one tenth of Q_{LH}. Sufficiently large Q_{SH} (>100Wm^{-2}) appears only in the boreal winter, in regions associated with the Kuroshio and Gulf Stream and Extensions and the northern North Atlantic (60°N–80°N). The sum of latent and sensible heat fluxes (Q_{LH}+Q_{SH}) accounts for the total turbulent oceanic heat loss to the atmosphere. As Q_{SH} is small and its spatial distribution is similar to that of Q_{LH}, the pattern of Q_{LH}+Q_{SH} largely resembles the pattern of Q_{LH} but with slightly enhanced magnitude.

To assess the degree of the seasonal flux variability, Figs.1-3 include also the plots of the standard deviations (STD) of the climatological monthly means of Q_{LH}, Q_{SH}, and Q_{LH}+Q_{SH} that are computed from the following equation

$$\sigma = \sqrt{\frac{\sum_{n=1}^{N}(x_n - \bar{x})^2}{N-1}} \qquad (20)$$

where σ denotes the STD, and N is 12 (months). x represents the climatological (1958-2006) monthly-mean fields of Q_{LH}, Q_{SH}, and Q_{LH}+Q_{SH}, while $\bar{x}$ is the annual-mean field of the respective flux. As expected, the largest seasonal STDs in the three flux fields are all located over the Gulf Stream, the Kuroshio, and their Extensions. It is apparent that the surface heat flux has a greater variability over the Kuroshio system than over the Gulf Stream system.

In general, the patterns of the annual mean and seasonal variations of the OAFlux components are in good consistency with those constructed from ship-based climatological atlases (Bunker, 1976; Esbensen and Kushnir, 1981; Oberhuber, 1988; da Silva et al., 1994; Josey et al., 1999) and satellite based long-term means (Chou et al., 1997; Schulz et al., 1997; Kubota et al. 2002; Bentamy et al. 2003). The basic structure of the mean global heat flux distribution over the 49-year period is also consistent with the one constructed over the 25-period (1981-2005) from the first phase of the OAFlux project (Yu and Weller, 2007).

Zonal averages of the flux fields of Q_{LH}, Q_{SH}, and Q_{LH} + Q_{SH} over the period of 1958-2006 are shown in Fig.4. The seasonal variations are evident, and the magnitude is larger in the northern hemisphere than in the southern hemisphere. On the annual mean basis, Q_{LH} peaks in the subtropical regions, around 20° latitude of both hemispheres; while large values of Q_{SH} appear at high northern latitudes, resulting primarily from enhanced sensible heat losses in the boreal winter season.

4.2 Evaporation

Evaporation (*Evp*) at the sea surface releases to the atmosphere not only latent heat energy but also water vapor. *Evp* can be determined from Q_{LH} from the following relation: $Evp = Q_{LH} / \rho_w L_e$, where ρ_w is the density of sea water, and L_e is the latent heat of vaporization that can

be expressed as $L_e = (2.501 - 0.00237 \times SST) \times 1.0^6$. A 49-year time series of global *Evp* fields is then computed from the OAFlux Q_{LH} analysis.

The oceans are the source of 86% of the global evaporation and are a key component of the global water cycle. The OAFlux evaporation dataset contributes to the understanding of long-term variability of ocean water cycle (Yu, 2007), and the understanding of potential water cycle variability in relation to global climate change.

4.3 Basic variables

Latent and sensible heat fluxes are predominantly determined by a combination of wind speed and sea-air humidity/temperature gradients (Eqs.1-2). OAFlux produces optimized estimates for the four independent air-sea variables, i.e., wind speed at 10m (U), specific air humidity at 2m (q_a), air temperature at 2m (T_a), and SST (T_s). Monthly means of the four variables for January, July, and annual average over the 49-year period are shown in Figs.5-8, respectively. Also included in the figures are the seasonal STDs of the four fields.

The global wind speed field is characterized by banded structures: high wind speed ($>12 ms^{-1}$) over the high northern/southern latitudes during respective hemispheric wintertime, weak wind speed ($<6 ms^{-1}$) in the equatorial band with weak seasonal variability, trade winds with moderate magnitude ($\sim 8 ms^{-1}$) in the subtropical oceans with sufficient seasonal variations. On the other hand, the three variables, q_a, T_a, and T_s, all show a similar global distribution: higher values are in the tropical regions with the maxima over the warmest water pools and the values decrease poleward. The location of the pool of the warm water ($T_s > 28°C$ for the Indo-Pacific and $T_s > 26°C$ for the Atlantic) changes with season, and so are the locations of q_a and T_a maxima. Seasonally, the maximum vertical gradients of air-sea humidity/temperature occur over the Kuroshio, the Gulf Stream, and their extensions during the boreal wintertime. This is caused by the advection of cold dry air from the continents by the seasonally strong wind speed. Large latent and sensible heat fluxes are thus produced.

Zonal averages of the four variable fields during the period 1958-2006 are shown in Fig.9. The meridional structure of wind speed is featured by large seasonal variability in the northern hemisphere. The similar distribution of q_a, T_a, and T_s over the global oceans is, again, clearly displayed.

5. Comparison with COADS-based and NWP-reanalyzed fluxes

The OAFlux products are constructed not from a single data source, but from an optimal blending of satellite retrievals and NWP model outputs. The products are independent of the COADS ship-based flux climatological atlases (da Silva et al., 1994; Josey et al., 1999) because COADS air-sea variables are not used in the synthesis. They also differ from the NWP model fluxes in that NWP modeled surface meteorological variables are just part of input datasets for the synthesis, and the OAFlux procedure used the state-of-the-art COARE bulk flux algorithm 3.0 (Fairall et al. 2003).

But, how different are the fluxes produced from using different datasets and different approaches? To address this question, we compare Q_{LH}, Q_{SH}, and $Q_{LH} + Q_{SH}$ from OAFlux with those produced by three NWP reanalysis models (ERA40, NCEP1, and NCEP2) and two COADS ship-based climatological atlases from da Silva et al. (1994) and NOC (Josey et al., 1999). Because the analysis period and temporal resolution among the six products (OAFlux, NOC, COADS–da Silva, ERA40, NCEP1, and NCEP2) vary considerably, we focus on the mean comparison only. To do this, we composed the mean fields for each dataset using its maximum available years except for NCEP1. The latter has a continuous time series for nearly 60 years starting from 1948, but only the period from 1958 to 2006 that matches the OAFlux analysis period was used. The base period used in obtaining the mean of each of the six dataset is listed in Table 3.

The mean comparison of Q_{LH}, Q_{SH}, and $Q_{LH} + Q_{SH}$ from the six datasets is shown in Figs. 10-12, respectively. It is clear that, although the basic structure of global flux distribution is similar between the six mean fields, the magnitude of the fluxes varies with the dataset. For Q_{LH}, the magnitude of the OAFlux fluxes has a good agreement with thos and COADS–da Silva (denoted by COADS in the figures), which is a pleasant surprise given that the methodology, data source, data density, and even the base period used in analyzing the three mean maps are very different. On the other hands, the three model reanalyzed Q_{LH} (ERA40, NCEP1, and NCEP2) are all stronger than the three analyzed Q_{LH} (OAFlux, NOC, and COADS-da Silva); and the differences can be about 20-30 Wm^{-2} in the subtropical oceans. By contrast, the mean Q_{SH} value is small and the differences between the products are also smaller except for NCEP2. In the latter, Q_{SH} over the Gulf Stream, the Kuroshio, and their extension is much stronger than

other products, while Q_{SH} over the ocean interior basins and at high southern latitudes are comparatively weaker. The differences in the six long-term mean Q_{LH} + Q_{SH} fields resemble those of the mean Q_{LH} fields.

The consistency between the six products is further shown in the plot of zonally averaged mean quantities (Fig.13). The OAFlux estimates have an overall good agreement with NOC and COADS-da Silva, and the differences between the three products are within 6 Wm^{-2} for the global regions north of 60°S. By comparison, the OAFlux estimates are consistently weaker than the three NWP reanalyses. The maximum difference in Q_{LH} occurs in the subtropics of the two hemispheres, where OAFlux Q_{LH} is weaker than NWP values by 20-30Wm^{-2}. ERA40 and NCEP1 also have also larger Q_{SH}, though their differences with the other analyzed Q_{SH} are comparatively smaller. Broadly speaking, NCEP2 Q_{LH} is strongest among all the products.

6. Comparison with in situ buoy measurements

The COADS-based climatological atlases provide a good long-term mean reference, but they cannot be regarded as the "truth" without further validation datasets. This is due to the fact that data coverage is uneven, and data are hardly available in regions such as the south oceans where there are no commercial ship routes. The validation datasets used in the OAFlux analysis are the flux buoy measurements acquired from the WHOI Improved METeorological instruments (IMET) (e.g. Moyer and Weller, 1997) at various sites, the TAO/TRITON buoy array in the tropical Pacific (McPhaden et al. 1998) and Indian Oceans (McPhaden et al. 2006), and the PIRATA in the tropical Atlantic Ocean (Servain et al. 1998). The location and time period of the total of 105 buoys used in the validation analysis are listed in Table 4. Two ship observations were included, one is the JASMINE in the Indian Ocean (Webster et al., 2002) and the other is the Labrador Sea Experiment (The Labrador Sea Group, 1998). Together with the 105 buoy locations, there are a total of 107 buoy daily time series.

The buoy comparison was made for OAFlux and the three NWP model fluxes. The mean differences between the product and buoy for Q_{LH}, Q_{SH}, and Q_{LH} + Q_{SH} are shown in Figs. 14-16, respectively. Warm colors indicate positive bias (i.e., the product is overestimated), and cold colors indicate negative bias (i.e., the product is underestimated). For NCEP2 Q_{LH} buoy comparison, warm colored dots predominate over almost all the locations – obviously NCEP

overestimates the latent heat release from the ocean. NCEP1 underestimates Q_{LH} in the tropical Pacific but overestimates Q_{LH} in the tropical and north Atlantic. ERA40 shows the similar tendency, albeit with a slightly lesser degree of bias. OAFlux Q_{LH} has a slight underestimation (overestimation) bias in the tropical Pacific (Atlantic), but across the board, it represents good improvement over all three NWP modeled Q_{LH}.

OAFlux Q_{SH} is well produced, showing no obvious bias. By comparison, ERA40 and NCEP1 Q_{SH} have an overall overestimation bias, NCEP2 Q_{SH}, however, shows an overall underestimation bias. The pattern of the product-minus-buoy for $Q_{LH} + Q_{SH}$ looks very similar to that for Q_{LH}, suggesting the bias in Q_{LH} is a major source of error for oceanic heat fluxes.

The mean product-minus-buoy values averaged over the 107 time series (105 buoys plus 2 ships) are listed in Table 5. The comparison is based on two criteria, one is the mean average of the differences between product and buoy over the 107 locations and the other is the absolute mean average of the product-buoy differences over the 107 locations. The former criterion is a measure of bias. If positive and negative differences cancel out each other, then the value is small. Otherwise, the product is biased. The latter criterion is a representation of the variance, indicating how the product is scattered from the buoy measurements. Even if the product is unbiased, the absolute mean can still be large if the product differs considerably from the buoy.

The two criteria show that OAFlux is unbiased and has the smallest variance. The mean OAFlux $Q_{LH} + Q_{SH}$ differs from the buoy mean by 1.0 Wm^{-2}, and the absolute mean difference is of 7.4Wm^{-2}. On the other hand, all NWP $Q_{LH} + Q_{SH}$ have overestimation bias and the absolute differences range from 11.4 Wm^{-2} for ERA40, to 17.3 Wm^{-2} for NCEP1, and to 23.1 Wm^{-2} for NCEP2. It is clear that NCEP2 fluxes are biased most – this is consistent with its comparison with NOC and COADS-da Silva (Figs.10-13).

7. Error estimation

The OAFlux estimation of latent and sensible heat fluxes is achieved through optimal blending of surface meteorological datasets from satellites and NWP reanalyses. The optimal blending is subject to weighted objective analysis, in which the weights are pre-determined. The variable estimates are sensitive to weights in regions where input data sources have large uncertainties and are less dependent of weights in regions where input data sets have good

accuracy (Yu et al. 2004). This suggests the accuracy of the OAFlux optimization is influenced by the accuracy of the input datasets.

Error estimates for daily latent and sensible heat fluxes and basic variables are computed based on the assumptions that the errors from one input data source is uncorrelated with the errors from another input data source, and that, at a given location and a given day, the accuracy of the variable estimate depends on how scatter the various input data are. Deviation of the error estimate is provided in Appendix A. Here the monthly mean error (standard deviation) maps for the two fluxes and the four basic variables averaged over the 49-year period are shown in Figs.17-23.

8. Summary

This report supports the third release of surface heat flux products developed by the Objectively Analyzed air-sea Heat Fluxes (OAFlux) project at the Woods Hole Oceanographic Institution (WHOI). The first version of the OAFlux products was made for the Atlantic Ocean (1988-1999) and the daily gridded datasets were released in March 2004. The second version of the OAFlux datasets was for the global oceans for the 1981-2002 period, and daily and monthly products were available online in December 2005. This third release is for the 1-degree gridded OAFlux global latent and sensible heat fluxes, ocean evaporation, and flux-related surface meteorological variables for the years 1958 to 2006.

The WHOI OAFlux product is constructed not from a single data source, but from an optimal blending of multi-platform satellite retrievals and three numerical weather prediction (NWP) reanalyses. The optimal blending is made to daily estimates of basic surface meteorological variables (i.e., wind speed, specific air/sea humidities and temperatures) by applying an advanced objective analysis. The optimally estimated variables are then utilized to compute daily flux fields from the COARE bulk flux algorithm version 3.0. This report documents the methodology, strategy, procedure, and input data sources used in developing the 49-year time series of global air-sea heat fluxes.

The report includes comparisons with two ship-based climatological atlase and three NWP reanalyzed fluxes. The long-term mean of latent plus sensible heat fluxes from OAFlux has good agreement with ship-based climatologies, but is consistently weaker than NWP

reanalyzed fluxes over the global oceans. The differences between OAFlux and NWP products can be as large as 20-30Wm^{-2} in the subtropical oceans. Comparisons with 107 (105 buoys plus 2 ships) in situ flux time series shows that OAFlux is unbiased and has smallest mean error: the mean OAFlux-buoy difference is of 1.0 Wm^{-2} and the mean difference in absolute measure is of 7.4 Wm^{-2}. By contrast, all three NWP turbulent heat fluxes show overestimation bias, with NCEP2 being the most biased: the mean NCEP2-buoy difference is more than 20Wm^{-2} when averaged over the 107 in situ measurement locations.

Monthly latent and sensible heat fluxes and related variables on 1-degree resolution are available for the entire 49-year period, while daily products are available from 1985 onward. The datasets are freely available to interested users for non-commercial scientific research. For further information, please visit the project website at http://oaflux.whoi.edu/. The OAFlux project is sponsored by NOAA Office of Climate Observation.

Acknowledgements

The project is supported by NOAA through the Cooperative Institute for Climate and Oceanic Research (CICOR) at the Woods Hole Oceanographic Institution (WHOI). The supporting NOAA Grants come from the Office of Climate Observations (OCO) and Climate Change Data and Detection (CCDD). We thank the following data centers for providing the data essential for our flux analysis: the OI daily SST analysis provided by the NOAA National Climate Data Center (ftp://eclipse.ncdc.noaa.gov/pub/OI-daily/NetCDF/); satellite wind products from the Remote Sensing Systems Company (http://www.ssmi.com); Version 2 of the Goddard Satellite-Based Surface Turbulent Fluxes (GSSTF) dataset from the NASA Goddard Earth Sciences Data and Information Services Center (http://disc.sci.gsfc.nasa.gov/); NCEP1 and NCEP2 Reanalysis data from the NOAA/OAR/ESRL Physical Science Division (http://www.cdc.noaa.gov/); ECMWF reanalyses from the Data Support Section at NCAR; the WHOI buoy datasets from the WHOI Upper Ocean Processes group (http://uop.whoi.edu); and the TAO/TRITON, PIRATA, and Indian Ocean buoy datasets maintained by NOAA/PMEL (http://www.pmel.noaa.gov/tao/). We thank Chris Fairall for providing the COARE3.0 algorithm.

References

Atlas, R., R. Hoffman, S. Bloom, J. Jusem, J. Ardizzone, 1996: A Multi-year Global Surface Wind Velocity Data Set Using SSM/I Wind Observations. *Bull. Amer. Meteor. Soc.*, **77**, 869-882.

Bentamy, A., K. B. Katsaros, A. M. Mestas-Nuñez, W. M. Drennan, E. B. Forde, and H. Roquet, 2003: Satellite estimates of wind speed and latent heat flux over the global oceans. *J. Climate*, **16**, 637-656.

Bergthorsson, P., and B. Döös, 1955: Numerical weather map analysis. *Tellus*, **7**, 329-340.

Bradley, E. F., C. W. Fairall, J. E. Hare, and A. A. Grachev, 2000: An old and improved bulk algorithm for air-sea fluxes: COARES2.6a. *AMS 14th Symposium on Boundary Layers and Turbulence*. Aspen, Colorado.

Bretherton, F. P., R. E. Davis, and C. B. Fandry, 1976: A technique for objective analysis and design of oceanographic experiment applied to MODE-73. *Deep-Sea Res.*, **23**, 559-582.

Brunke, M. A., X. Zeng, and S. Anderson (2002), Uncertainties in sea surface turbulent flux algorithms and data sets, *J. Geophys. Res.*, **107**(C10), 3141, doi:10.1029/2001JC000992.

Bunker, A. F., 1976: Computations of surface energy flux and annual air-sea interaction cycles of the North Atlantic Ocean. *Mon. Wea. Rev.*, **104**, 1122-1140.

Cayan, D. R., 1992a: Latent and sensible heat flux anomalies over the Northern Oceans: The connection to monthly atmospheric circulation. *J. Climate*, **5**, 354-369.

Cayan, D. R., 1992b: Latent and sensible heat flux anomalies over the Northern Oceans: Driving the sea surface temperature. *J. Phys. Oceanogr*., **22**, 859-881.

Cayan, D. R., 1992c: Variability of latent and sensible heat fluxes estimated using bulk formulae. *Atmosphere-Ocean*, **30**, 1-42.

Chou, S. -H., R. Atlas, C. -L. Shie, and J. Ardizzone, 1995: Estimates of surface humidity and latent heat fluxes over oceans from SSMI data. *Mon. Wea. Rev.*, **123**, 2405-2425.

Chou, S.-H., C.-L. Shie, R. M. Atlas and J. Ardizzone, 1997: Air-sea fluxes retrieved from Special Sensor Microwave Imager data. *J. Geophys. Res.,* **102**, 12705-12726.

Chou, S.-H., E. J. Nelkin, J. Ardizzone, R. M. Atlas, and C.-L. Shie, 2001: Goddard Satellite-based Surface Turbulent Fluxes (GSSTF) – Version 2 Documentation. Distributed Active Archive Center (DAAC), NASA Goddard Space Flight Center, Greenbelt, Maryland.

Curry, J. A., C. A. Clayson, W. B. Rossow, R. Reeder, Y. C. Zhang, P. J. Webster, G. Liu, and R. S. Sheu, 1999: High-resolution satellite-derived dataset of the ocean surface fluxes of heat, freshwater and momentum for the TOGA COARE IOP. *Bull. Amer. Meteorol. Soc.,* **80**, 2059-2080.

da Silva, A. M., C. C. Young, S. Levitus, 1994: *Atlas of Surface Marine Data. Vol. 3: Anomalies of Heat and Momentum Fluxes.* NOAA Atlas NESDIS vol. 8, 413 pp. U.S. Gov. Print. Off. Washington, D. C.

Daley, R., 1991: *Atmospheric Data Analysis*. Cambridge University Press. 457pp.

Ebuchi, N., H. C. Graber, and M. J. Caruso, 2002: Evaluation of wind vectors observed by QuikSCAT/SeaWinds using ocean buy data. *J. Atmos. Oceanic Technol.*, **19**, 2049– 2062.

Esbensen, S. K., and V. Kushnir, 1981: *The heat budget of the global oceans: An atlas based on estimates from marine surface observations*. Oregon State University Climate Research Institute Rep. 29.

Fairall, C. W., E. F. Bradley, J. S. Godfrey, G.A. Wick, J. B. Edson, and G. S. Young, 1996a: The cool skin and the warm layer in bulk flux calculations. *J. Geophys. Res.* 101, 1295-1308.

Fairall, C. W., E. F. Bradley, D. P. Rogers, J. B. Edson, and G. S. Young, 1996b: Bulk parameterization of air–sea fluxes for Tropical Ocean-Global Atmosphere Coupled–Ocean Atmosphere Response Experiment. *J. Geophys. Res.,* **101**, (C2) 3747–3764.

Fairall, C. W., E. F. Bradley, J. E. Hare, A. A. Grachev, and J. B. Edson, 2003: Bulk parameterization on air–sea fluxes: Updates and verification for the COARE algorithm. *J. Climate.,* **16**, 571–591.

Hsiung, J., 1985. Estimates of global oceanic meridional heat transport. *J. Phys. Oceanogr.*, **15**, 1405-1413.

Isemer, H. -J., and L. Hasse, 1985: *The Bunker Climate Atlas of the North Atlantic Ocean: 1. Observations.* Springer-Verlag, 218pp.

Isemer H.J. and L. Hasse, 1987: *The Bunker climate atlas of the North Atlantic Ocean: 2. Air-sea interactions*. Springer-Verlag, 256pp

Josey, S. A., E. C. Kent, and P. K. Taylor, 1998: The Southampton Oceanography Centre (SOC) Ocean-Atmosphere Heat, Momentum and Freshwater Flux Atlas. Southampton Oceanography Centre Rep.6, Southampton, United Kingdom, 30pp + figures.

Josey, S. A., E. C. Kent, and P. K. Taylor, 1999: New insights into the ocean heat budget closure problem from analysis of the SOC air-sea flux climatology. *J. Climate*, **12**, 2850-2880.

Josey, S. A., 2001: A comparison of ECMWF and NCEP/NCAR surface heat fluxes with moored buoy measurements in the subduction region of the North-East Atlantic. *J. Climate*, **14**, 1780-1789.

Kalnay, E., and coauthors, 1996: The NCEP/NCAR 40-year reanalysis project. *Bull. Amer. Meteor. Soc.,* **77**, 437-471.

Kanamitsu, M., W. Ebisuzaki, J. Woolen, J. Potter and M. Fiorino, 2002: NCEP/DOE AMIP-II Reanalysis (R-2). *Bull.Amer. Met. Soc.* **83**, 1631-1643.

Kubota, M., N. Iwasaka, S. Kizu, M. Konda, and K. Kutsuwada, 2002: Japanese Ocean Flux data dets with Use of Remote sensing Observations (J-OFURO). *J. Oceanogr.*, **58**, 213–225.

Legler, D. M., I. M. Navon, and J. J. O'Brien, 1989: Objective analysis of pseudostress over the Indian ocean using a direct-minimization approach. *Mon. Wea. Rev.*, **117**, 709-720.

Liu, W. T., K. B. Katsaros, and J. A. Businger, 1979: Bulk parameterization of air–sea exchanges of heat and water vapor including the molecular constraints at the interface. *J. Atmos. Sci.,* **36**, 1722–1735.

McPhaden, M. J., A. J. Busalacchi, R. Cheney, J. R. Donguy, K. S. Gage, D. Halpern, M. Ji, P. Julian, G. Meyers, G. T. Mitchum, P. P. Niiler, J. Picaut, R. W. Reynolds, N. Smith, K.

Takeuchi, 1998: The Tropical Ocean-Global Atmosphere (TOGA) observing system: A decade of progress. *J. Geophys. Res.*, **103**, 14,169-14,240.

McPhaden, M. J., Y. Kuroda, and V. S. N. Murty, 2006: Development of an Indian Ocean moored buoy array for climate studies. *CLIVAR Exchanges*, **11**(4), 3-5, International CLIVAR Office, Southampton, UK.

Moyer, K. A., and R. A. Weller, 1997: Observations of surface forcing from the Subduction Experiment: A comparison with global model products and climatological datasets. *J. Climate*, **10**, 2725-2742.

Oberhuber, J. M., 1988: An atlas based on COADS data set: The budget of heat, buoyancy and turbulent kinetic energy at the surface of the Global Ocean. MPI Rep. 15, 1999pp.

Reynolds, R. W., N. A. Rayner, T. M. Smith, D. C. Stokes and W. Wang, 2002: An improved in situ and satellite SST analysis for climate. *J. Climate*, **15**, 1609-1625.

Reynolds, R.W., T.M. Smith, C. Liu, D.B. Chelton, K.S. Casey, and M.G. Schlax, 2007: Daily High-Resolution-Blended Analyses for Sea Surface Temperature. *J. Climate*, **20**, 5473–5496.

Schulz, J., P. Schlüssel, and H. Graßl, 1993: Water vapor in the atmospheric boundary layer over oceans from SSM/I measurements. *Int. J. Remote Sens.*, **14**, 2773-2789.

Schulz, J., J. Meywerk, S. Ewald, and P. Schlussel, 1997: Evaluation of satellite-derived latent heat fluxes. *J. Climate*, **10**, 2782-2795.

Servain, J., A. J. Busalacchi, M. J. McPhaden, A. D. Moura, G. Reverdin, M. Vianna, and S. E. Zebiak, 1998: A Pilot Research Moored Array in the Tropical Atlantic (PIRATA). *Bull. Am. Meteorol. Soc.*, **79**, 2019-2031.

Sun, B., L. Yu, and R. A. Weller, 2003: Comparisons of surface meteorology and turbulent heat fluxes over the Atlantic: NWP model analyses versus moored buoy observations. *J. Climate*, **14**, 679-695.

The Labrador Sea Group, 1998: The Labrador Sea Deep Convection Experiment. *Bull. Amer. Meteorol. Soc*. **79**, 2033-2058.

Toole, J.M., H.M. Zhang, and M.J. Caruso, 2004: Time-Dependent Internal Energy Budgets of the Tropical Warm Water Pools. *J. Climate*, **17**, 1398–1410.

Uppala, S.M., and co-authors, 2005: The ERA-40 re-analysis. *Quart. J. R. Meteorol. Soc*., **131**, 2961-3012.doi:10.1256/qj.04.176.

Webb, E.K., G.I. Pearman and R. Leuning, 1980: Correction of flux measurements for density effects due to heat and water vapour transfer, *Q.J.R. Meteorol. Soc.* 106, 85-100.

Webster, P. J., E. F. Bradley, C. W. Fairall, J. S. Godfrey, P. Hacker, R. A. Hopuze jr., R. Lukas, Y. Serra, J. M. Hummon, T. D. M. Lawrence, C. A. Russel, M. N. Ryan, K. Sahami, P. Zuidema, 2002: The Joint Air-Sea Monsoon Interaction Experiment (JASMINE) Pilot Study. *Bull. Amer. Met. Soc*., **83**, 1603-1630.

Webster, P., and R. Lukas, 1992: TOGA-COARE The Coupled Ocean-Atmosphere Response Experiment. Bull. Amer. Meteor. 73, 1377-1416.

Weller, R. A., M. F. Baumgartner, S. A. Josey, A. S. Fischer, and J. Kindle, 1998: Atmospheric forcing in the Arabian Sea during 1994-1995: observations and comparisons with climatology and models. *Deep Sea Res*., **45**(11), 1961-1999.

Wentz, F. J., 1997: A well-calibrated ocean algorithm for SSM/I. *J. Geophys. Res.*, **102**, 8703-8718.

Woodruff, S. D., H. F. Diaz, J. D. Elms, and S. J. Worley, 1998: COADS Release 2 data and metadata enhancements for improvements of marine surface flux fields. *Phys. Chem. Earth*, **23**, 517-526.

Xie, P., and P. A. Arkin, 1996: Analyses of global monthly precipitation using gauge observations, satellite estimates and numerical model predictions. *J. Climate*, **9**, 840-858.

Yu, L., and J .J. O'Brien, 1991: Variational estimation of the wind stress drag coefficient and the oceanic eddy viscosity profile. *J. Phys. Oceanogr.,* **21**, 709-719.

Yu, L., and J. J. O'Brien, 1995: Variational data assimilation for determining the seasonal net surface heat flux using a tropical Pacific Ocean model. *J. Phys. Oceanogr.*, **25**, 2319-2343.

Yu, L., R. A. Weller, and B. Sun, 2004a: Improving latent and sensible heat flux estimates for the Atlantic Ocean (1988-1999) by a synthesis approach. *J. Climate*, **17**, 373-393.

Yu, L**.**, R. A. Weller, and B. Sun, 2004b: Mean and variability of the WHOI daily latent and sensible heat fluxes at in situ flux measurement sites in the Atlantic Ocean. *J. Climate*, **17**, 2096-2118.

Yu, L., X. Jin, and R.A. Weller, 2006: Role of Net Surface Heat Flux in Seasonal Variations of Sea Surface Temperature in the Tropical Atlantic Ocean. *J. Climate*, **19**, 6153–6169.

Yu, L., X. Jin, and R.A. Weller, 2007: Annual, Seasonal, and Interannual Variability of Air–Sea Heat Fluxes in the Indian Ocean. *J. Climate*, **20**, 3190–3209.

Yu, L., and R.A. Weller, 2007: Objectively analyzed air–sea heat fluxes for the global ice-free oceans (1981–2005). *Bull. Amer. Meteor. Soc.*, **88**, 527–539.

Yu, L., 2007. Global variations in oceanic evaporation (1958-2005): The role of the changing wind speed. *J. Climate*, **20**, 5376-5390.

Table captions

Table 1. Input data sources and available periods. Purple color denotes satellite-based product and black color denotes NWP-based product. The OAFlux start time is marked at the bottom of the table, and the start times for daily and monthly products are also indicated.

Table 2. Scaling parameters assigned to the weighting matrices.

Table 3. The base period used in constructing the long-term mean for each of the six flux data sets.

Table 4. List of the location, available time period, and total number of days of the time series used in validation analysis. There are a total of 107 time series, of which 105 are from buoys and two are from ships.

Table 5. Mean differences between product and buoy averaged over 107 buoy time series based on two criteria: the mean average (denoted by $\sum$) and the absolute mean average (denoted by $\sum$abs).

Figure captions

Fig.1 Latent heat flux (Q_{LH}) averaged over the period 1958-2006. (Top left) monthly mean in January; (Top right) monthly mean in July; (Bottom left) annual mean; and (Bottom right) seasonal standard deviation (STD).

Fig.2 Same as Fig.1 but for sensible heat flux (Q_{SH}).

Fig.3 Same as Fig.1 but for latent plus sensible heat fluxes (Q_{LH}+Q_{SH}).

Fig.4 Zonally averaged (Top left) latent heat flux (Q_{LH}), (top right) sensible heat flux (Q_{SH}), and (bottom) latent plus sensible heat fluxes (Q_{LH}+Q_{SH}) over the period 1958-2006.

Fig.5 Same as Fig.1 but for wind speed at 10m (U).

Fig.6 Same as Fig.1 but for specific air humidity at 2m (q_a).

Fig.7 Same as Fig.1 but for air temperature at 2m (T_a).

Fig.8 Same as Fig.1 but for sea surface temperature (T_s).

Fig.9 Zonally averaged (top left) wind speed at 10m (U), (top right) specific air humidity at 2m (q_a), (bottom left) air temperature at 2m (T_a), and (bottom right) sea surface temperature (T_s) over the period 1958-2006.

Fig.10. Comparison of long-term mean latent heat flux (Q_{LH}) produced by OAFlux, NOC, COADS-da Silva (denoted by COADS), ERA40, NCEP1, and NCEP2. The base period used in constructing the mean of each of the six datasets is listed in Table 4.

Fig.11 Same as Fig.10 but for Q_{SH}.

Fig.12 Same as Fig.10 but for Q_{LH}+Q_{SH}.

Fig.13 Comparison of zonally averaged (Top left) latent heat flux (Q_{LH}), (top right) sensible heat flux (Q_{SH}), and (bottom) latent plus sensible heat fluxes (Q_{LH}+Q_{SH}) produced from six flux data sources.

Fig.14 Mean Q_{LH} comparison (product-minus-buoy) at the 105 buoy locations. The mean difference at each location represents the average over the available measurement period.

Fig.15 Same as Fig.14 but for Q_{SH}.

Fig.16 Same as Fig.14 but for Q_{LH}+Q_{SH}.

Fig.17 Estimated monthly mean error (standard deviation) for Q_{LH} for (Top right) January, (Top left) July, and (Bottom) annual average. The fields are the average over the 49-year (1958-2006) period.

Fig.18 Same as Fig.17 but for Q_{SH}.

Fig.19 Same as Fig.17 but for $Q_{LH} + Q_{SH}$.

Fig.20 Same as Fig.17 but for U.

Fig.21 Same as Fig.17 but for q_a.

Fig.22 Same as Fig.17 but for T_a.

Fig.23 Same as Fig.17 but for T_s.

Table 1. Input data sources and available periods. Purple color denotes satellite-based product and black color denotes NWP-based product. The OAFlux start time is marked at the bottom of the table, and the start times for daily and monthly products are also indicated.

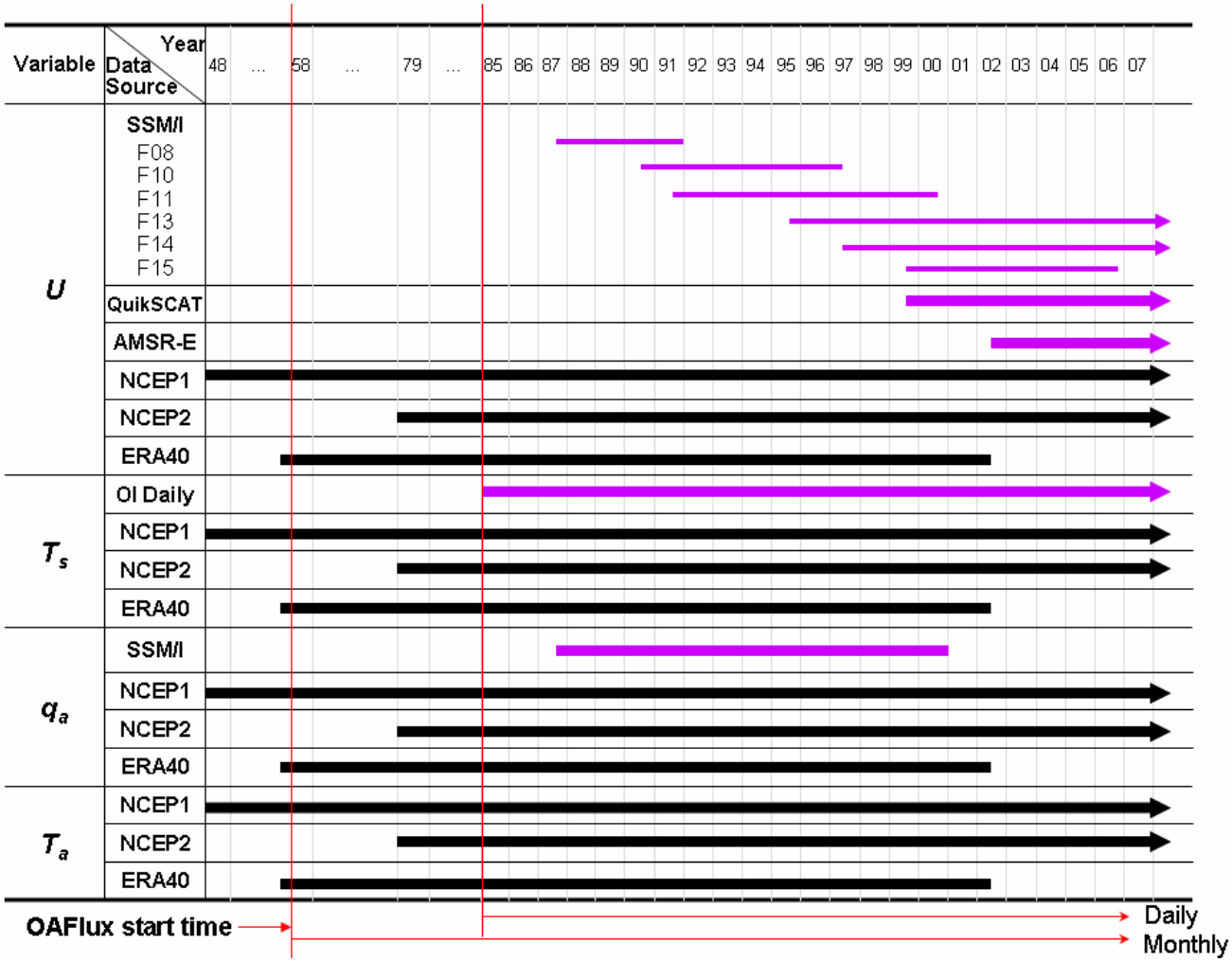

Table 2. Scaling parameters assigned to the weighting matrices

Weights \ Data	NCEP1	NCEP2	ERA40	SSMI	QSCAT	AMSRE	OI Daily SST	GSSTF2
$R(U)$	1	1	1	4	4	4		
$R(T_s)$	1		1				2	
$R(q_a)$	1	1	1.3					0.4
$R(T_a)$	1	1	2					

Table 3. The base period used in constructing the long-term mean for each of the six flux data sets

Data	Base period	No. of Years
OAFlux	1958 - 2006	49
NOC	1980 - 2005	26
COADS – da Silva	1950 - 1993	44
ERA40	1958 - 2001	44
NCEP1	1958 - 2006	49
NCEP2	1979 - 2006	28

Table 4. List of the location, available time period*, and total number of days of the time series used in validation analysis. There are total 107 time series, of which 105 are from buoys and two are from ships.

* Note: Actual measurement period at some buoy locations is longer than listed below. The available time period denotes that this is the period that all the four basic variables (U, q_a, T_a, and T_s) have available measurements.

Buoys	Location	Time period	No. of days
Arabian Sea	(61.5E, 15.5N)	10/16/94 to 10/19/95	366
Indian Ocean	(80.5E, EQ)	07/25/93 to 12/31/06	425
Indian Ocean	(90.0E,1.5S)	10/23/01 to 06/08/04	643
Indian Ocean	(95.0E, 5.0S)	10/26/01 to 12/31/06	300
COARE	(156.0E, 1.8N)	10/22/92 to 03/03/93	133
PACS_north	(125.4W, 9.9N)	04/30/97 to 09/13/98	499
PACS_south	(124.6W, 2.8N)	04/21/97 to 09/19/98	514
Stratus	(85.0W, 20.0N)	10/08/00 to 12/11/04	1526
NTAS	(51.0W, 14.8N)	03/31/01 to 02/15/03	687
Subduction	(34.0W, 33.0N)	07/04/91 to 05/31/93	698
Subduction	(22.0W, 33.0N)	06/19/91 to 06/13/93	726
Subduction	(29.0W, 25.5N)	06/24/91 to 06/15/93	723
Subduction	(34.0W, 18.0N)	06/26/91 to 06/20/93	726
Subduction	(22.0W, 18.0N)	06/30/91 to 06/18/93	720
SMILE	(123.5W, 38.6N)	11/15/88 to 05/13/89	180
ASREX91	(132.0W, 49.2N)	11/01/91 to 01/06/92	67
ASRES93	(69.7W, 33.9N)	12/15/93 to 03/23/94	99
CMO	(70.5W, 40.5N)	07/31/96 to 06/12/97	317
SESMOOR	(61.2W, 42.5N)	10/18/88 to 03/07/89	141
MLML91	(20.8W, 59.5N)	04/30/91 to 09/05/91	129
WHOTS	(158.0W, 22.8N)	09/15/04 to 06/24/06	635
KEO	(145.0E, 32.0N)	06/17/04 to 10/15/06	650
PIRATA	(38.0W, 15.0N)	01/28/98 to 11/28/06	2312
PIRATA	(38.0W, 12.0N)	02/04/99 to 12/29/06	896
PIRATA	(38.0W, 8.0N)	01/31/98 to 11/25/06	1774
PIRATA	(38.0W, 4.0N)	04/12/02 to 12/02/06	1357
PIRATA	(35.0W, EQ)	01/22/98 to 11/29/05	1212
PIRATA	(23.0W, EQ)	03/07/99 to 12/29/06	1816
PIRATA	(10.0W. EQ)	08/16/99 to 12/29/06	813
PIRATA	(10.0W, 6.0N)	03/15/00 to 12/29/06	1119
PIRATA	(10.0W, 10.0N)	09/11/97 to 12/31/06	2637

PIRATA	(0.0E, EQ)	11/09/98 to 12/29/06	873
PIRATA	(23.0W, 4.0N)	06/12/06 to 12/29/06	108
PIRATA	(23.0W, 12.0N)	06/09/06 to 12/29/06	183
PIRATA	(34.0W, 19.0N)	09/01/05 to 11/02/06	428
PIRATA	(32.0W, 14.0N)	08/24/05 to 11/04/06	438
PIRATA	(30.0W, 8.0N)	08/21/05 to 06/26/06	310
PIRATA	(8.0E, 6.0N)	06/29/06 to 12/29/06	184
TAO	(165.0E, 8.0N)	08/28/92 to 08/25/96	648
TAO	(180.0E, 8.0N)	11/23/93 to 11/08/01	1727
TAO	(170.0W, 8.0N)	08/21/92 to 10/10/01	1883
TAO	(155.0W, 8.0N)	03/06/93 to 10/06/01	2331
TAO	(125.0W, 8.0N)	09/13/96 to 08/29/01	1466
TAO	(110.0W, 8.0N)	03/10/93 to 11/16/99	1366
TAO	(95.0W, 8.0N)	08/12/97 to 08/16/99	734
TAO	(156.0E, 5.0N)	09/11/92 to 07/22/06	2863
TAO	(165.0E, 5.0N)	04/20/94 to 08/29/97	583
TAO	(180.0E, 5.0N)	03/25/93 to 01/26/01	1578
TAO	(170.0W, 5.0N)	11/14/93 to 06/13/01	1212
TAO	(155.0W, 5.0N)	07/23/91 to 10/05/01	2511
TAO	(140.0W, 5.0N)	10/30/90 to 09/18/00	1317
TAO	(125.0W, 5.0N)	11/03/91 to 01/31/01	1860
TAO	(110.0W, 5.0N)	03/11/93 to 05/03/00	1224
TAO	(95.0W, 5.0N)	05/13/96 to 05/18/99	559
TAO	(156.0E, 2.0N)	07/29/96 to 12/29/06	2582
TAO	(165.0E, 2.0N)	04/18/94 to 03/15/97	970
TAO	(180.0E, 2.0N)	03/26/93 to 11/27/00	2560
TAO	(170.0W, 2.0N)	11/13/93 to 09/24/00	1234
TAO	(155.0W, 2.0N)	05/24/94 to 06/21/00	1166
TAO	(140.0W, 2.0N)	11/28/91 to 09/19/00	2323
TAO	(125.0W, 2.0N)	09/10/94 to 09/12/00	1343
TAO	(110.0W, 2.0N)	05/19/96 to 07/29/00	835
TAO	(95.0W, 2.0N)	11/14/92 to 03/23/97	800
TAO	(147.0E, EQ)	04/28/94 to 09/17/06	2410
TAO	(156.0E, EQ)	03/02/92 to 05/03/06	2900
TAO	(165.0E, EQ)	03/30/91 to 01/05/98	1054
TAO	(180.0E, EQ)	03/27/93 to 11/25/99	1877
TAO	(170.0W, EQ)	04/16/95 to 07/01/00	1186
TAO	(155.0W, EQ)	08/15/92 to 10/25/99	1458
TAO	(140.0W, EQ)	05/01/90 to 05/07/98	2169

TAO	(125.0W, EQ)	09/28/92 to 09/01/95	608
TAO	(110.0W, EQ)	05/09/93 to 01/31/98	845
TAO	(95.0W, EQ)	08/20/95 to 05/28/98	419
TAO	(137.0E, 2.0N)	04/30/93 to 08/14/05	1046
TAO	(147.0E, 2.0N)	05/02/92 to 12/21/06	2135
TAO	(156.0E, 2.0N)	02/22/93 to 04/09/06	2276
TAO	(165.0E, 2.0N)	08/22/92 to 01/04/98	1363
TAO	(180.0E, 2.0N)	03/28/93 to 06/26/96	750
TAO	(170.0W, 2.0N)	08/24/92 to 10/30/00	1571
TAO	(155.0W, 2.0N)	03/03/93 to 12/17/97	524
TAO	(140.0W, 2.0N)	05/03/92 to 12/31/06	4046
TAO	(125.0W, 2.0N)	05/04/93 to 04/25/98	1497
TAO	(110.0W, 2.0N)	11/04/92 to 09/19/99	1020
TAO	(95.0W, 2.0N)	11/16/92 to 05/29/98	412
TAO	(137.0E, 5.0N)	09/29/01 to 01/25/06	1185
TAO	(147.0E, 5.0N)	12/08/93 to 12/21/06	2076
TAO	(156.0E, 5.0N)	03/04/92 to 04.13.06	3047
TAO	(165.0E, 5.0N)	08/21/92 to 06/08/97	1302
TAO	(180.0E, 5.0N)	06/28/96 to 07/19/01	1151
TAO	(170.0W, 5.0N)	04/05/93 to 06/13/94	420
TAO	(155.0W, 5.0N)	07/18/91 to 06/01/01	2277
TAO	(140.0W, 5.0N)	10/24/90 to 09/15/99	1712
TAO	(125.0W, 5.0N)	12/07/91 to 04/15/95	654
TAO	(110.0W, 5.0N)	03/14/93 to 04/10/00	910
TAO	(95.0W, 5.0N)	05/09/96 to 05/23/99	434
TAO	(137.0E, 8.0N)	07/02/02 to 06/11/03	246
TAO	(156.0E, 8.0N)	02/10/97 to 02/17/06	1882
TAO	(165.0E, 8.0N)	09/05/90 to 06/02/97	1364
TAO	(180.0E, 8.0N)	11/30/93 to 03/18/01	848
TAO	(170.0W, 8.0N)	08/26/92 to 10/17/01	2452
TAO	(155.0W, 8.0N)	04/08/95 to 06/17/00	1098
TAO	(125.0W, 8.0N)	09/19/96 to 10/03/99	964
TAO	(110.0W, 8.0N)	10/24/98 to 11/09/99	382
TAO	(95.0E, 8.0N)	08/22/95 to 11/28/99	436
TAO	(140.0W, 9.0N)	05/25/94 to 09/13/99	1376

Table 5. Mean differences between product and buoy averaged over 107 buoy time series based on two criteria: the mean average (denoted by ∑) and the absolute mean average (denoted by ∑abs).

Mean Diff	Q_{LH} (Wm^{-2})	Q_{SH}(Wm^{-2})	$Q_{LH}+Q_{SH}$(Wm^{-2})
∑ (OAFlux – Buoy)	0.98	0.04	1.03
∑ (ERA40 – Buoy)	7.04	1.79	8.83
∑ (NCEP1 – Buoy)	3.71	2.62	6.33
∑ (NCEP2 – Buoy)	21.06	0.01	21.07
∑ abs(OAFlux – Buoy)	6.65	1.47	7.43
∑ abs(EAR40 – Buoy)	9.64	2.25	11.40
∑ abs(NCEP1 – Buoy)	14.44	3.97	17.34
∑ abs(NCEP2 – Buoy)	22.10	3.56	23.06

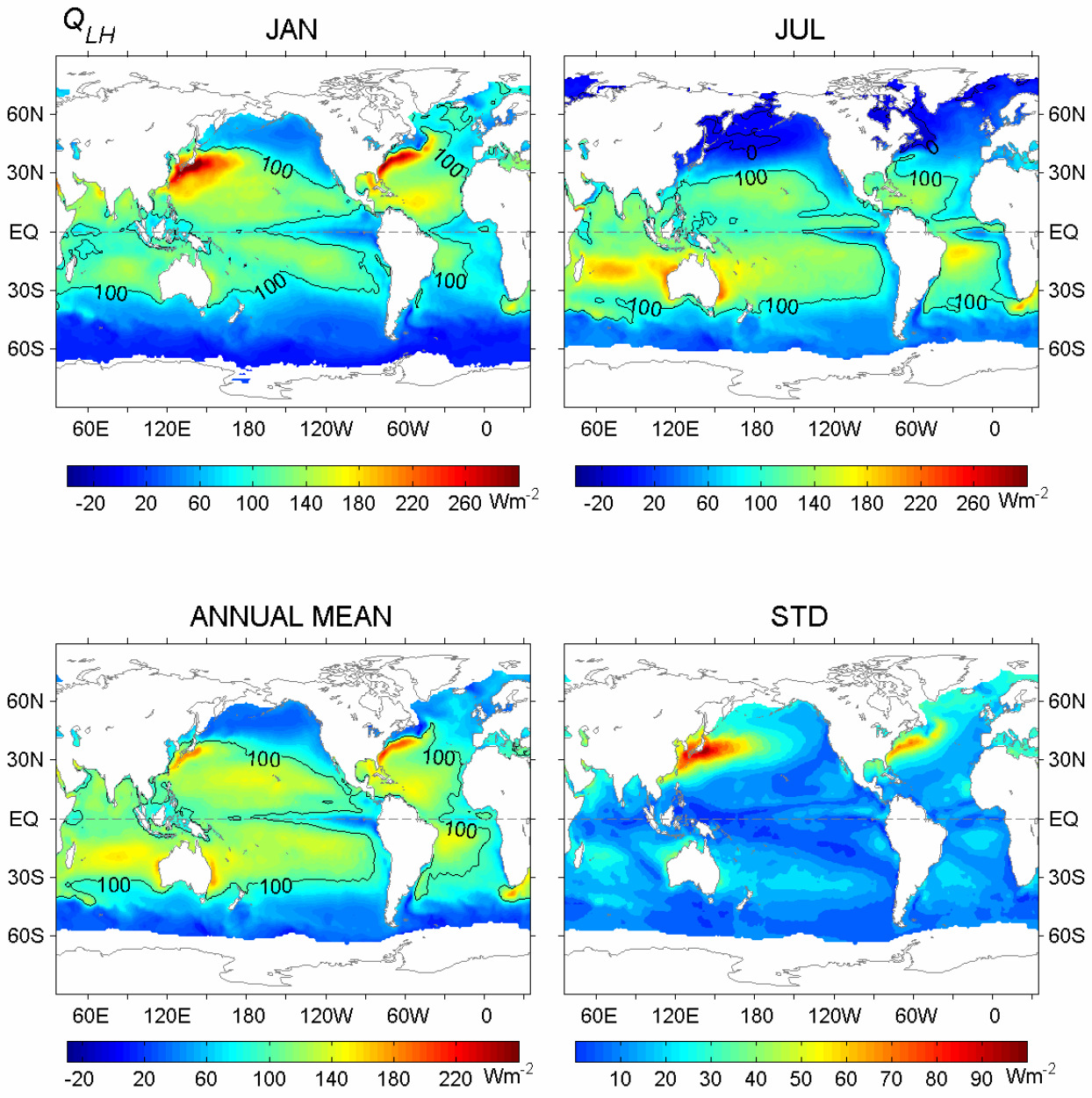

Fig.1 Latent heat flux (Q_{LH}) averaged over the period of 1958-2006. (Top left) monthly mean in January; (Top right) monthly mean in July; (Bottom left) annual mean; and (Bottom right) seasonal standard deviation (STD).

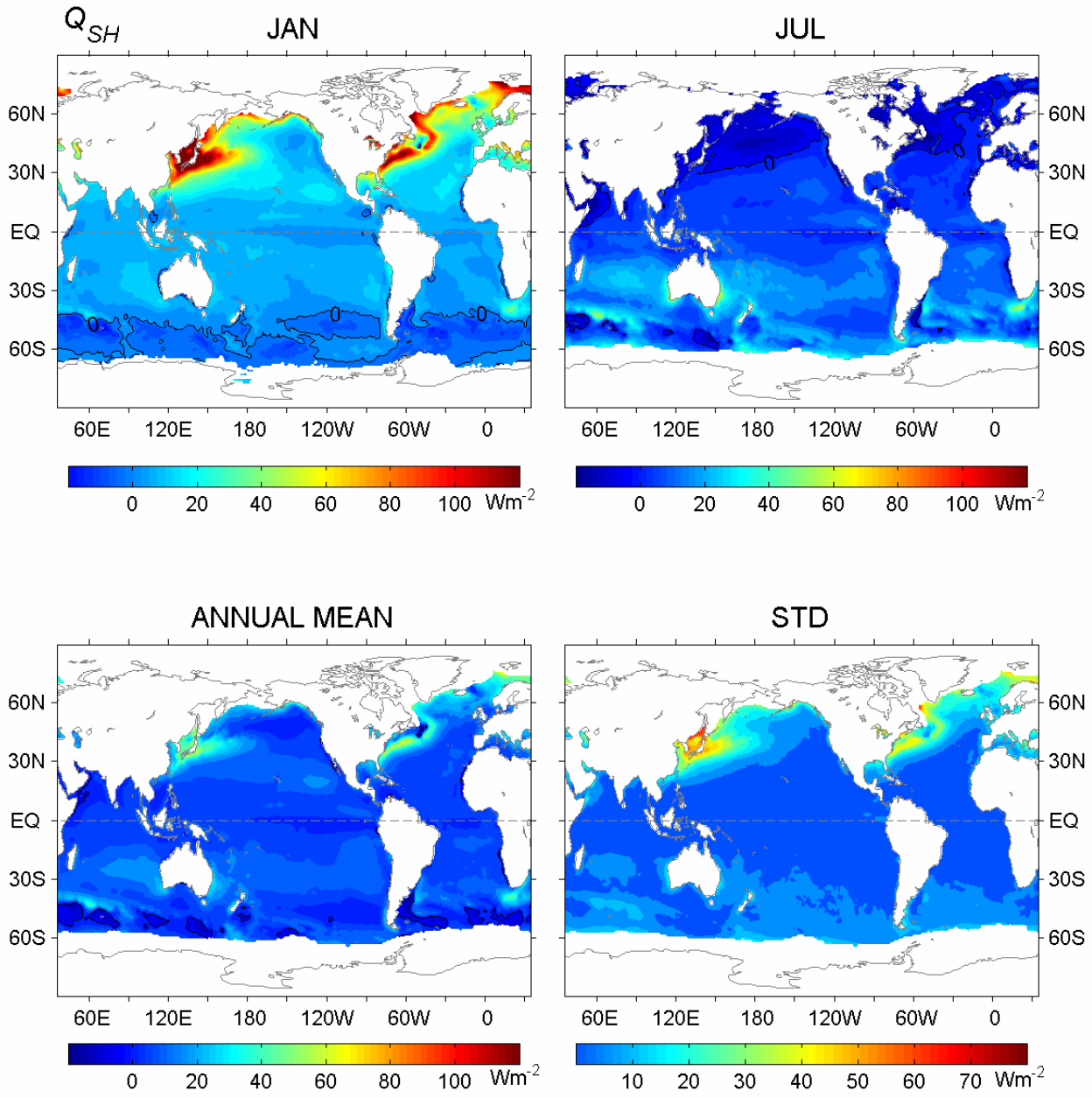

Fig.2 Same as Fig.1 but for sensible heat flux (Q_{SH}).

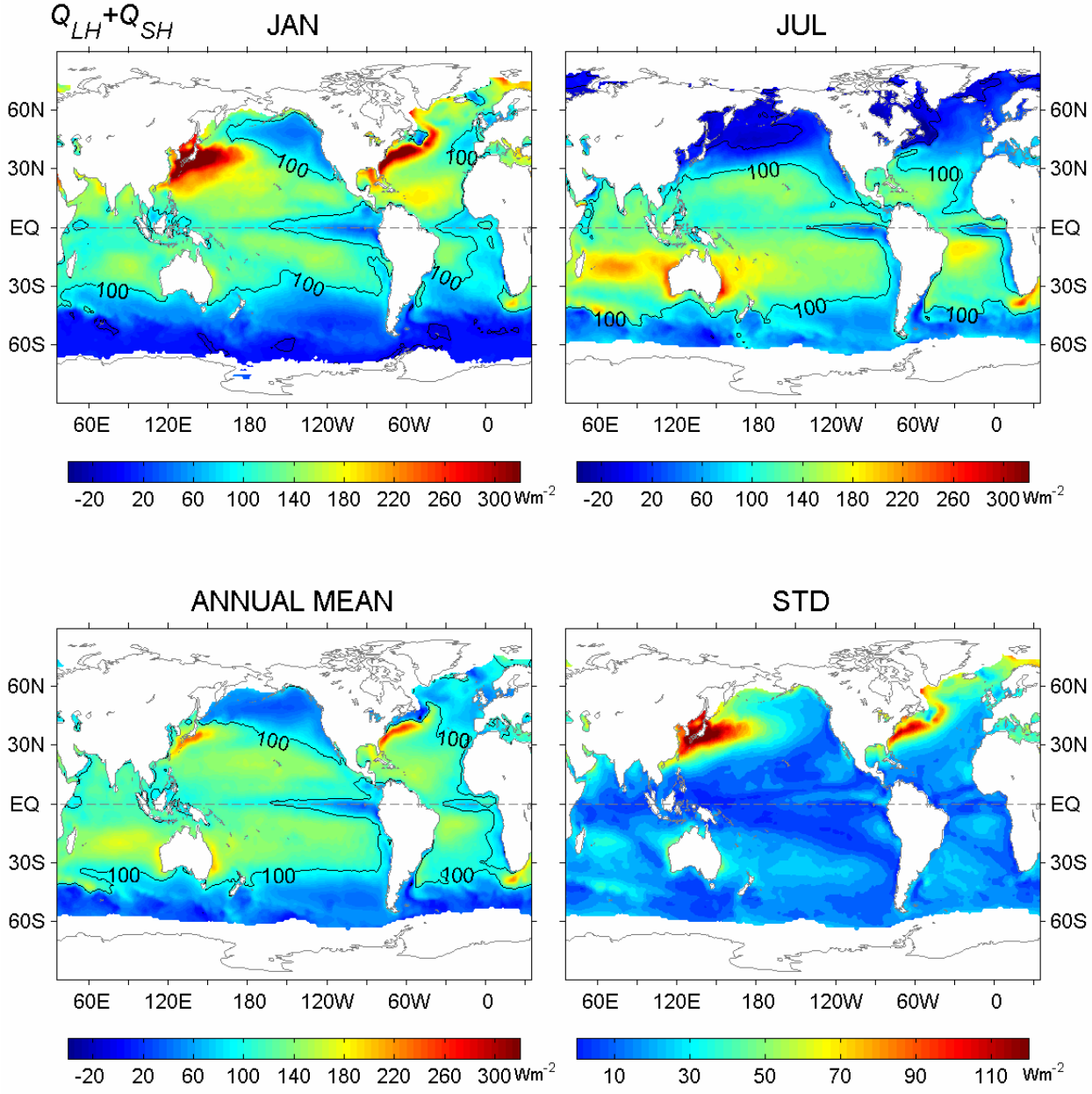

Fig.3 Same as Fig.1 but for latent plus sensible heat fluxes (Q_{LH}+Q_{SH}).

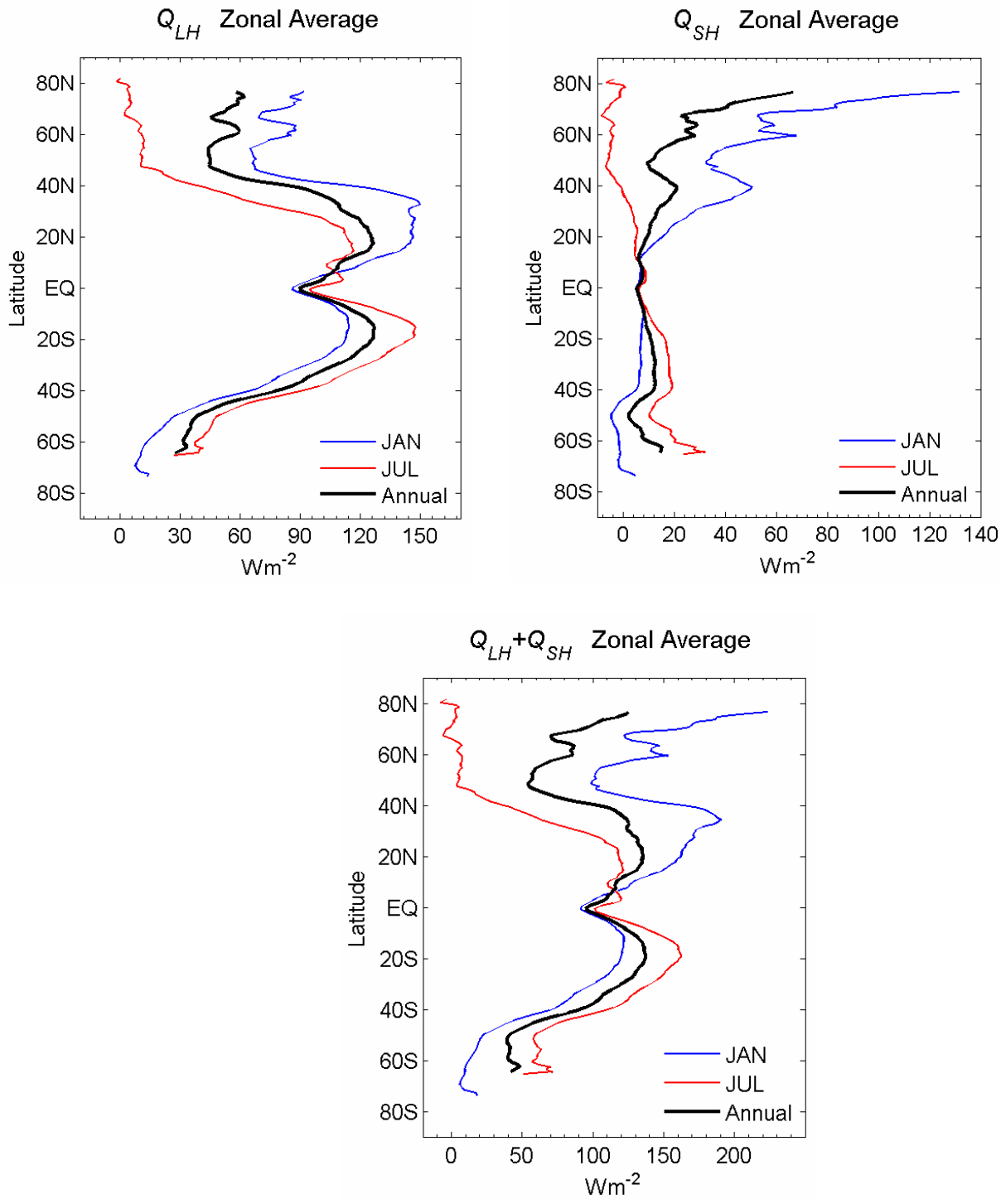

Fig.4 Zonally averaged (Top left) latent heat flux (Q_{LH}), (top right) sensible heat flux (Q_{SH}), and (bottom) latent plus sensible heat fluxes (Q_{LH}+Q_{SH}) over the period 1958-2006.

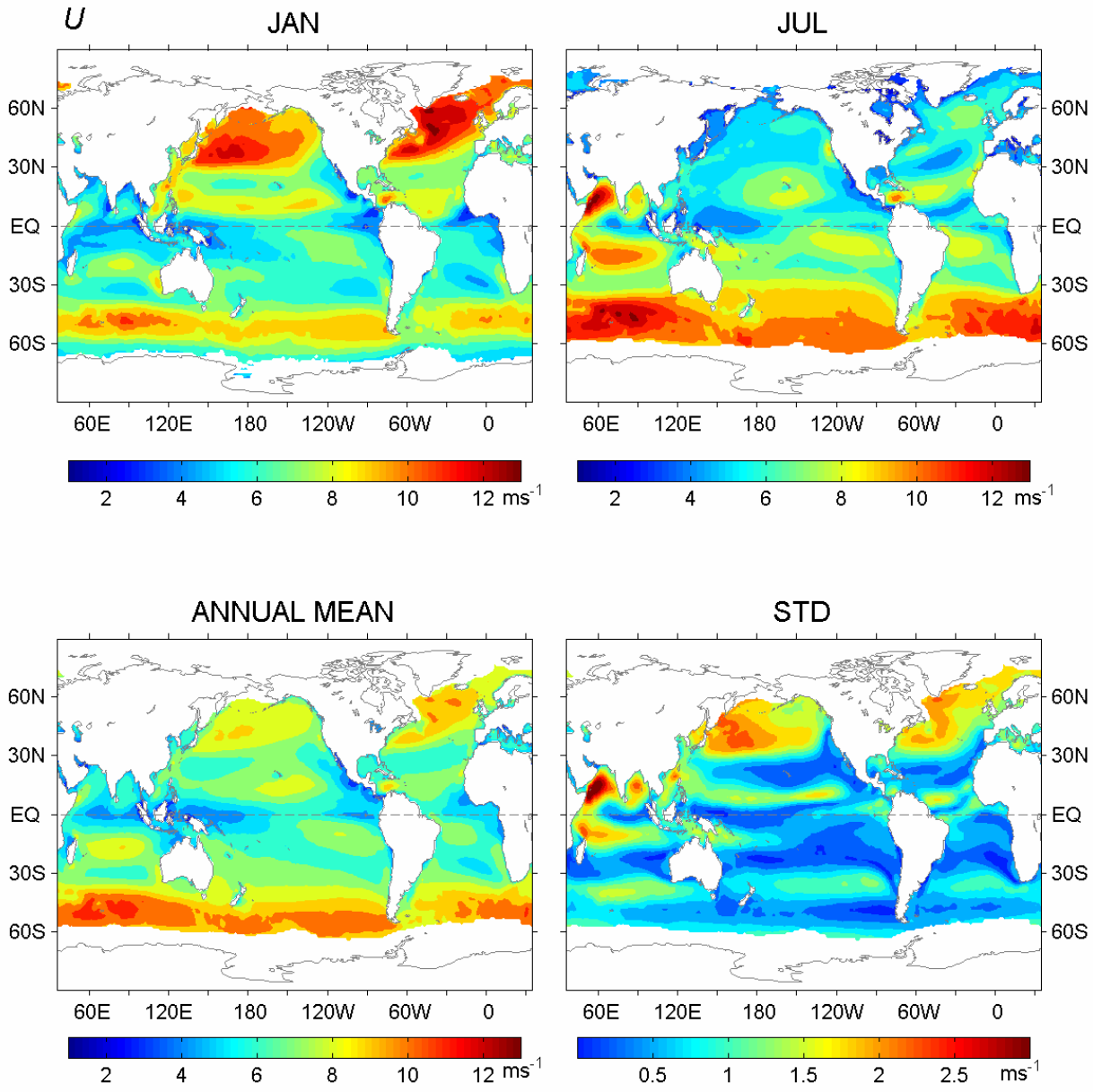

Fig.5 Same as Fig.1 but for wind speed at 10m (*U*).

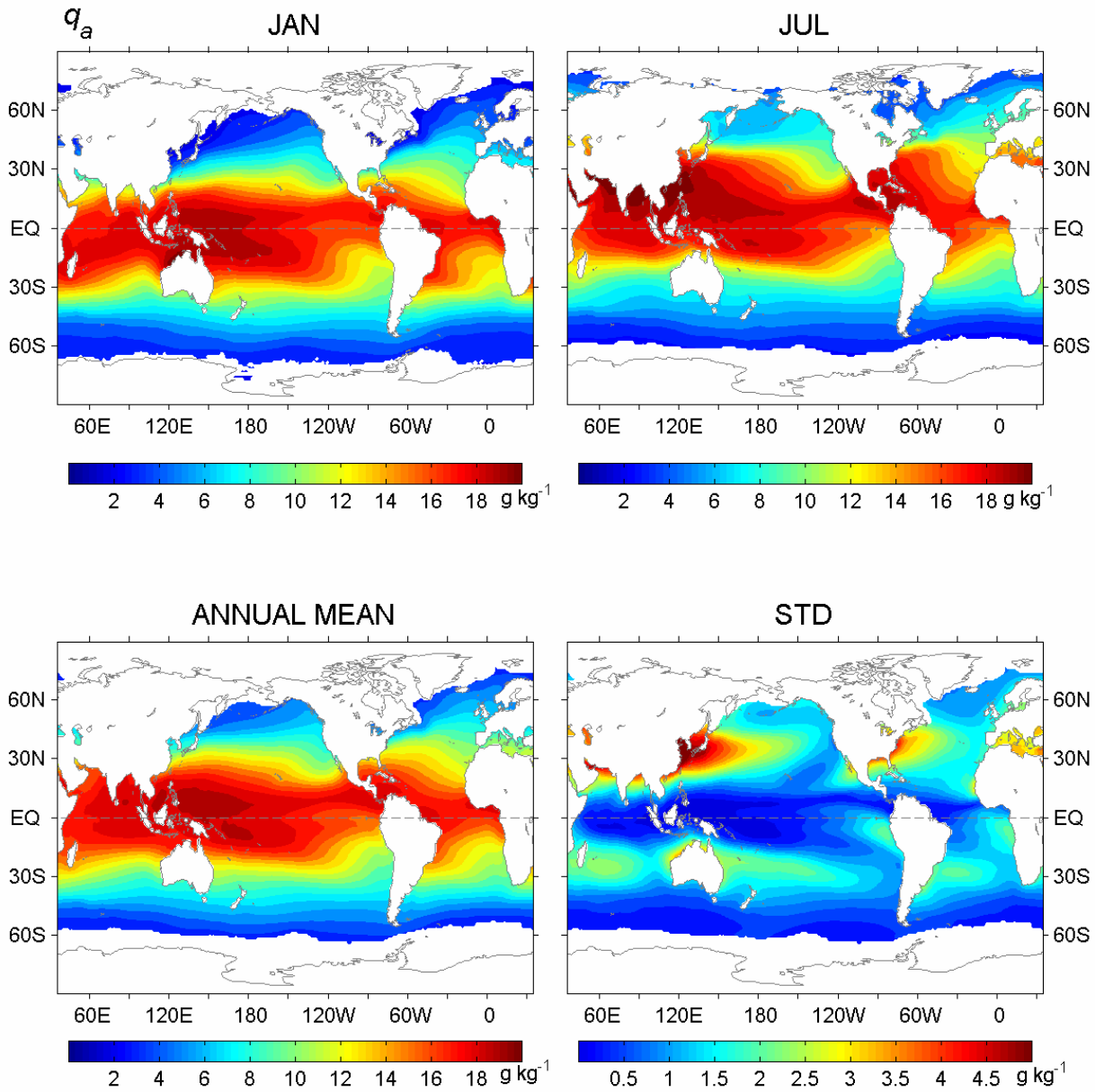

Fig.6 Same as Fig.1 but for specific air humidity at 2m (q_a).

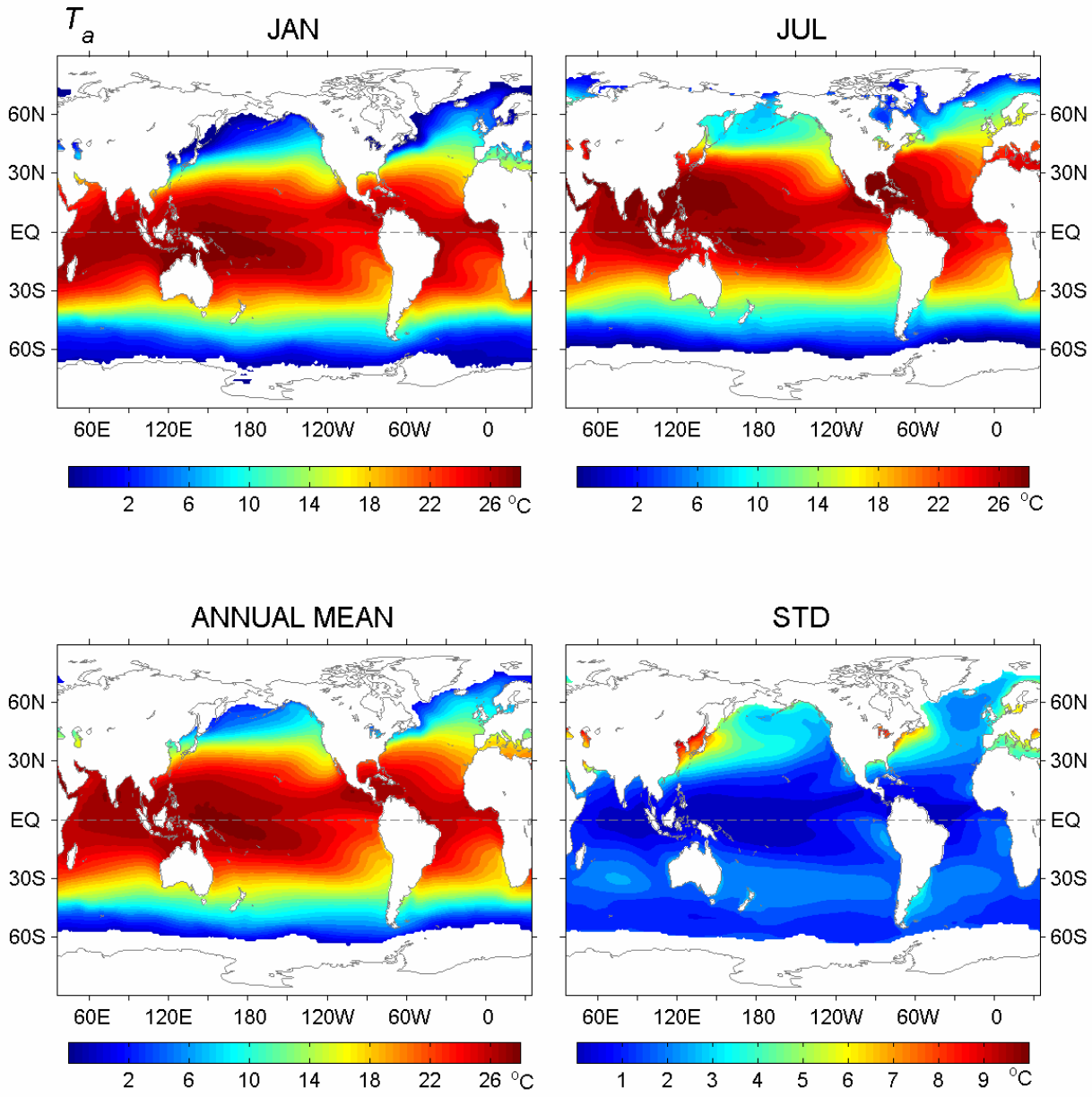

Fig.7 Same as Fig.1 but for air temperature at 2m (T_a).

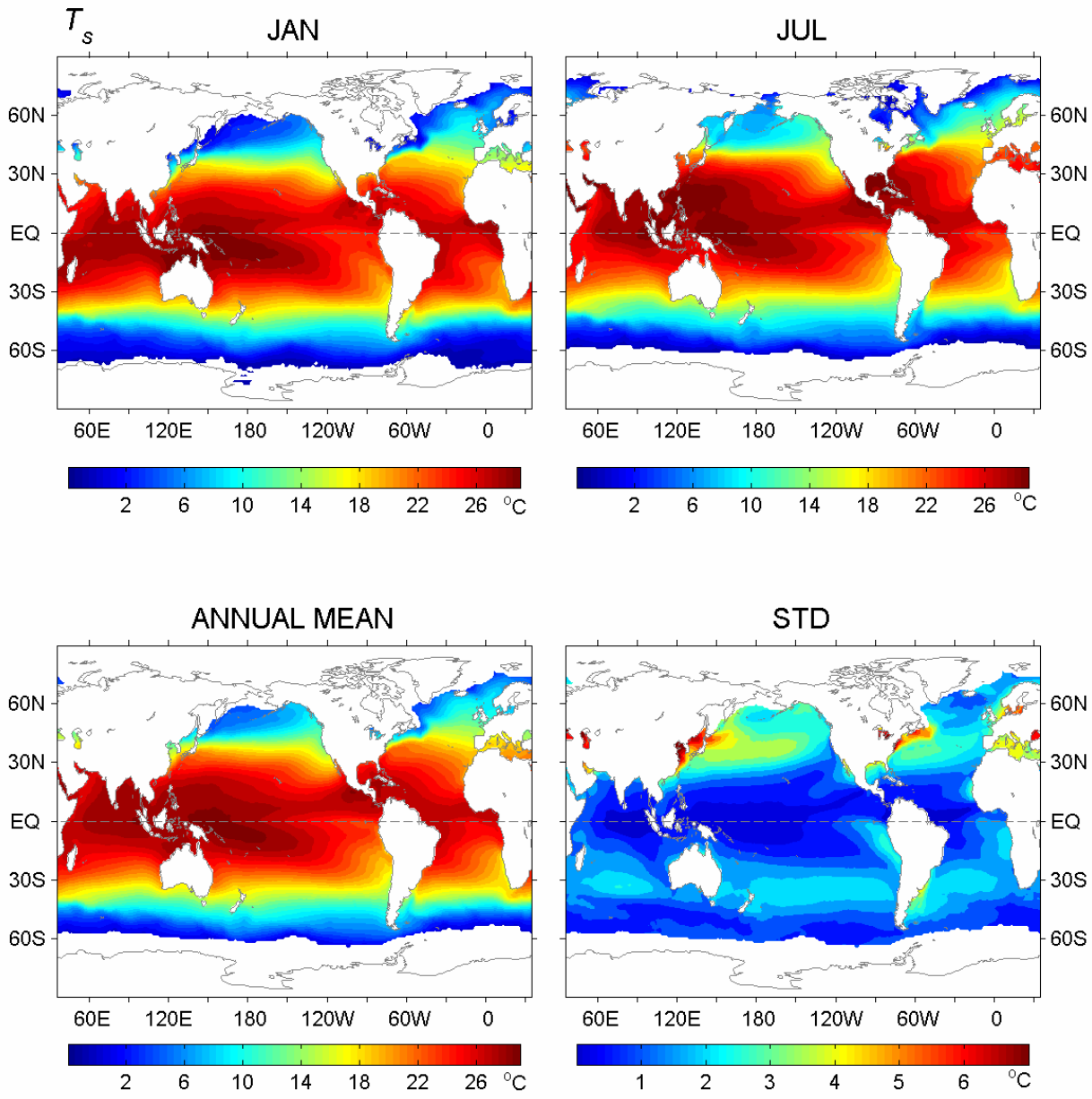

Fig.8 Same as Fig.1 but for sea surface temperature (T_s).

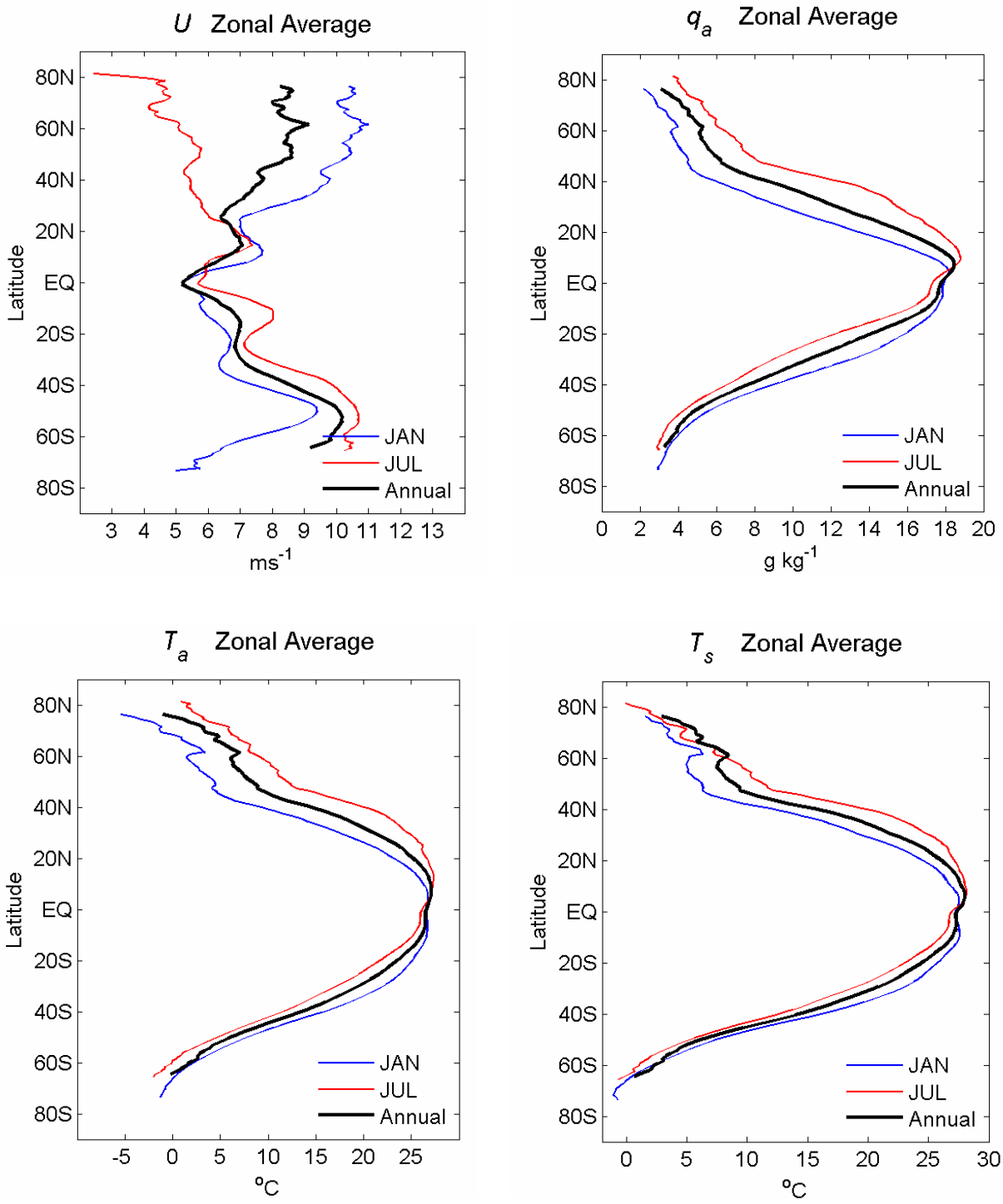

Fig.9 Zonally averaged (top left) wind speed at 10m (U), (top right) specific air humidity at 2m (q_a), (bottom left) air temperature at 2m (T_a), and (bottom right) sea surface temperature (T_s) over the period 1958-2006.

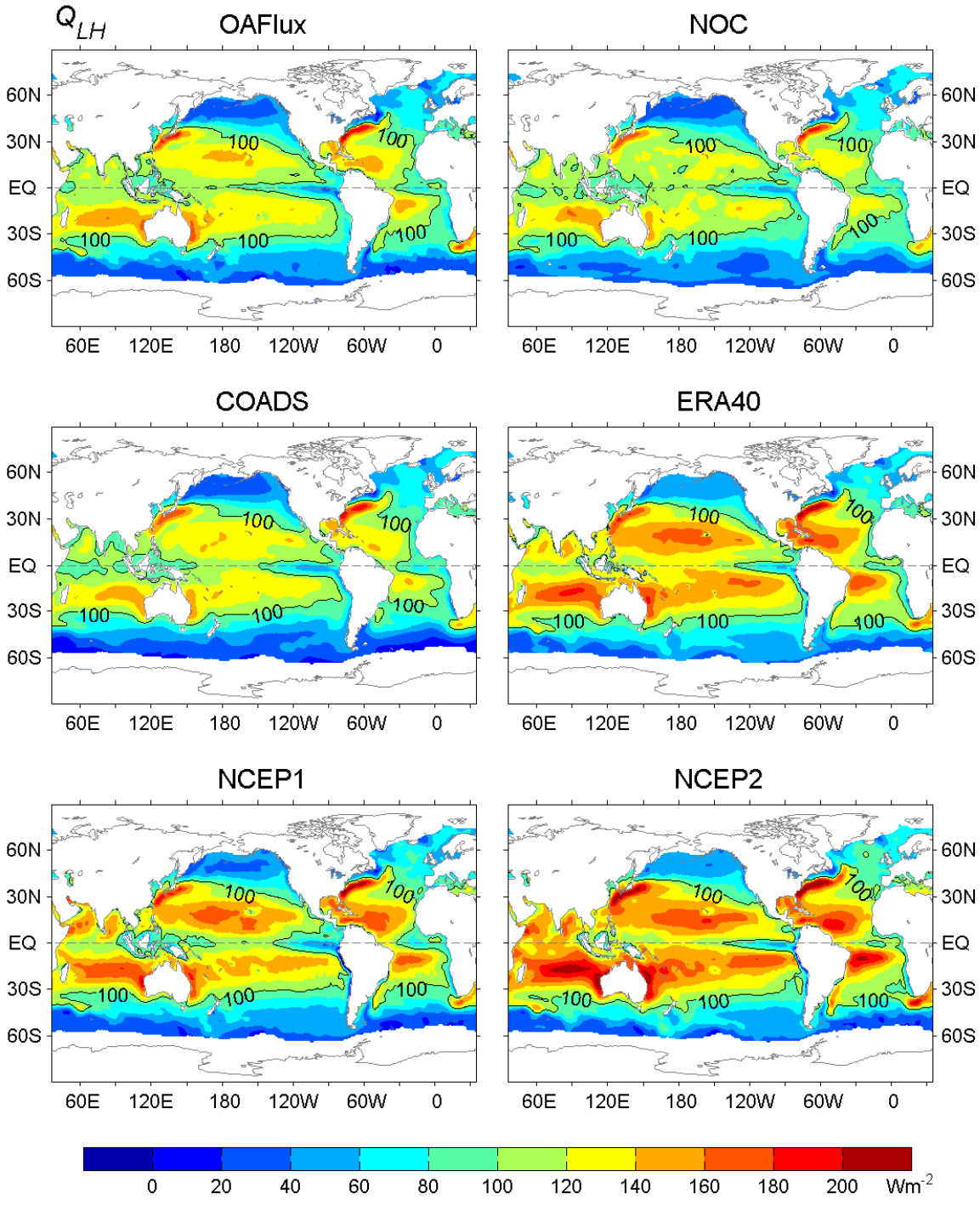

Fig.10. Comparison of long-term mean latent heat flux (Q_{LH}) produced by OAFlux, NOC, COADS-da Silva (denoted by COADS), ERA40, NCEP1, and NCEP2. The base period used in constructing the mean of each of the six datasets is listed in Table 4.

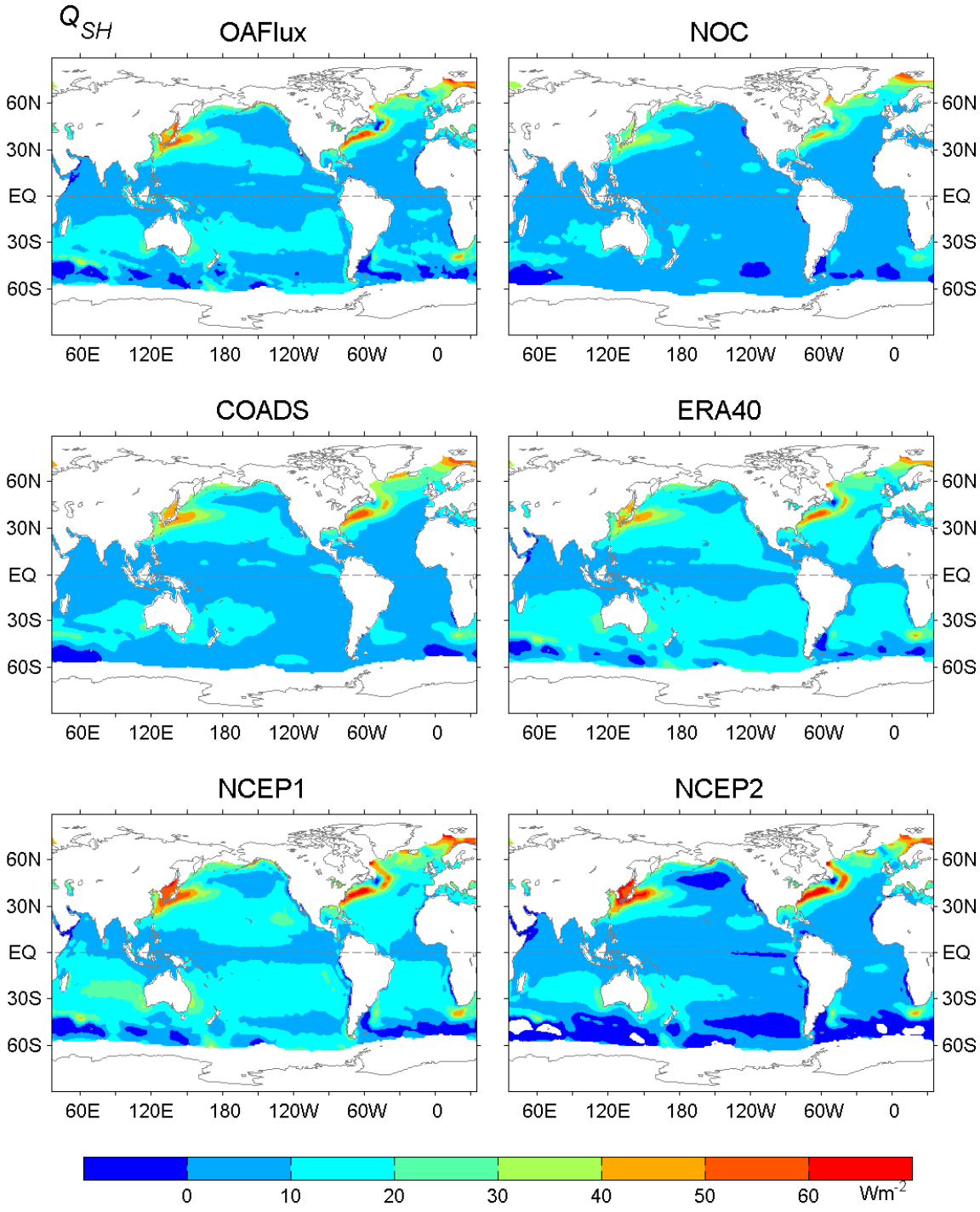

Fig.11 Same as Fig.10 but for Q_{SH}.

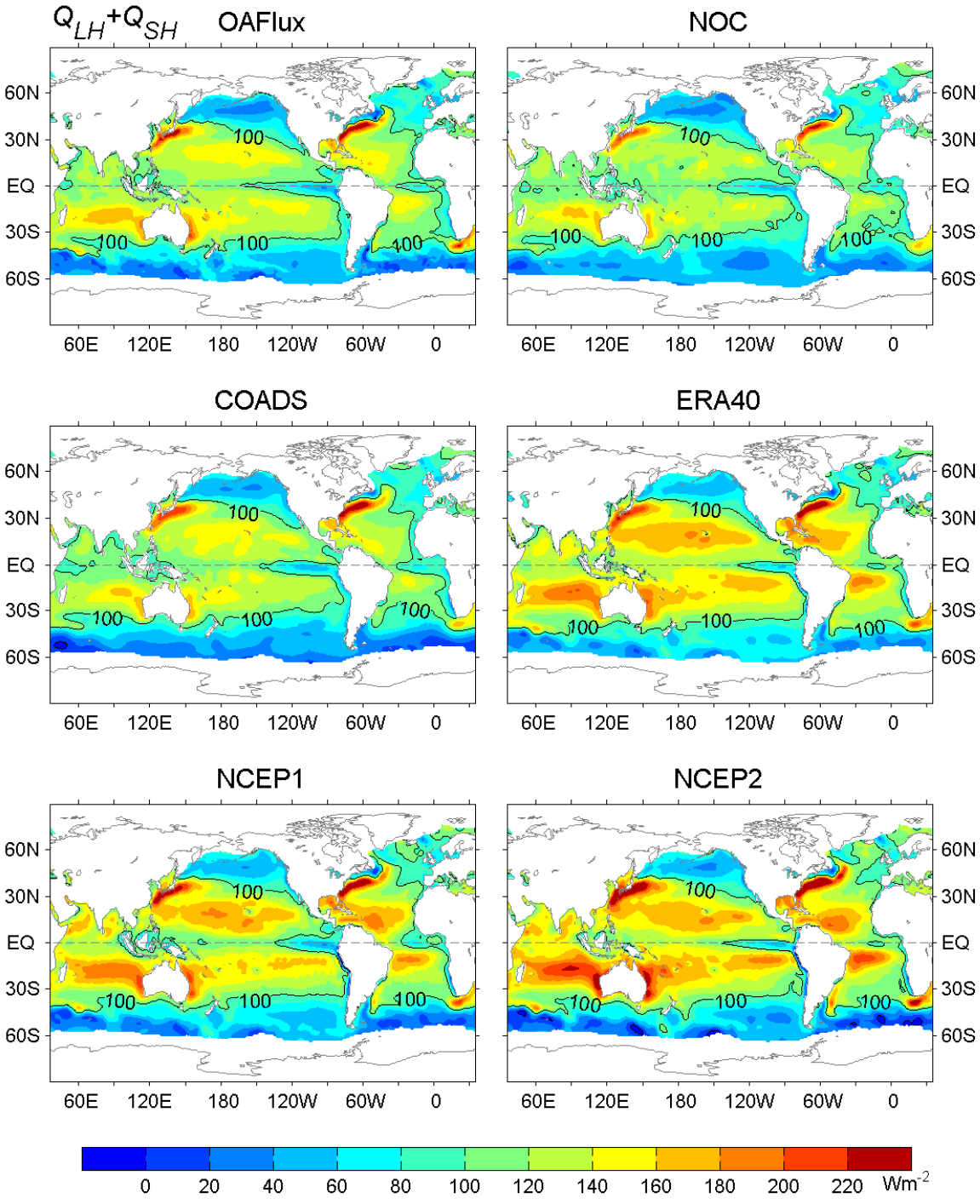

Fig.12 Same as Fig.10 but for $Q_{LH}+Q_{SH}$.

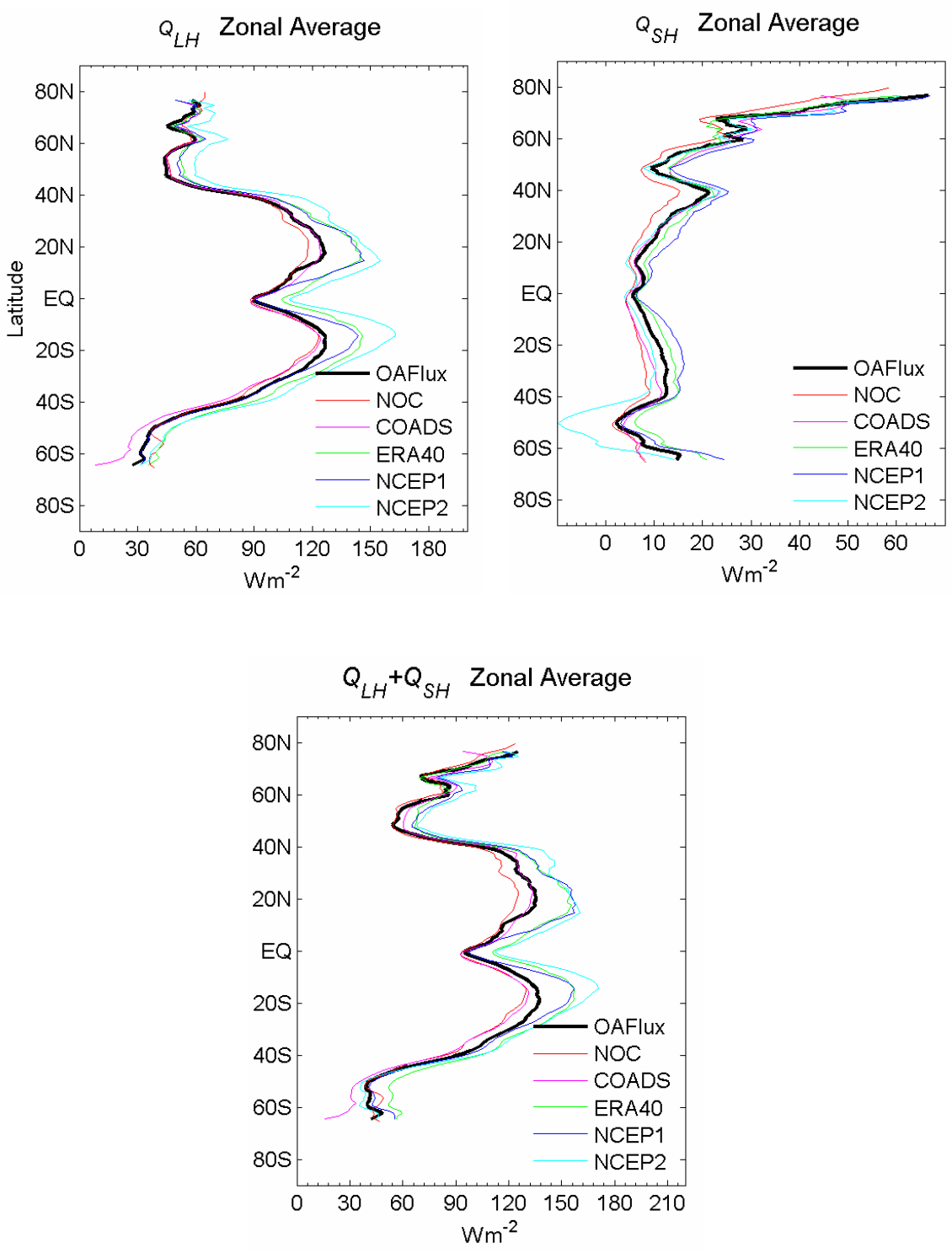

Fig.13 Comparison of zonally averaged (Top left) latent heat flux (Q_{LH}), (top right) sensible heat flux (Q_{SH}), and (bottom) latent plus sensible heat fluxes (Q_{LH}+Q_{SH}) produced from six flux data sources.

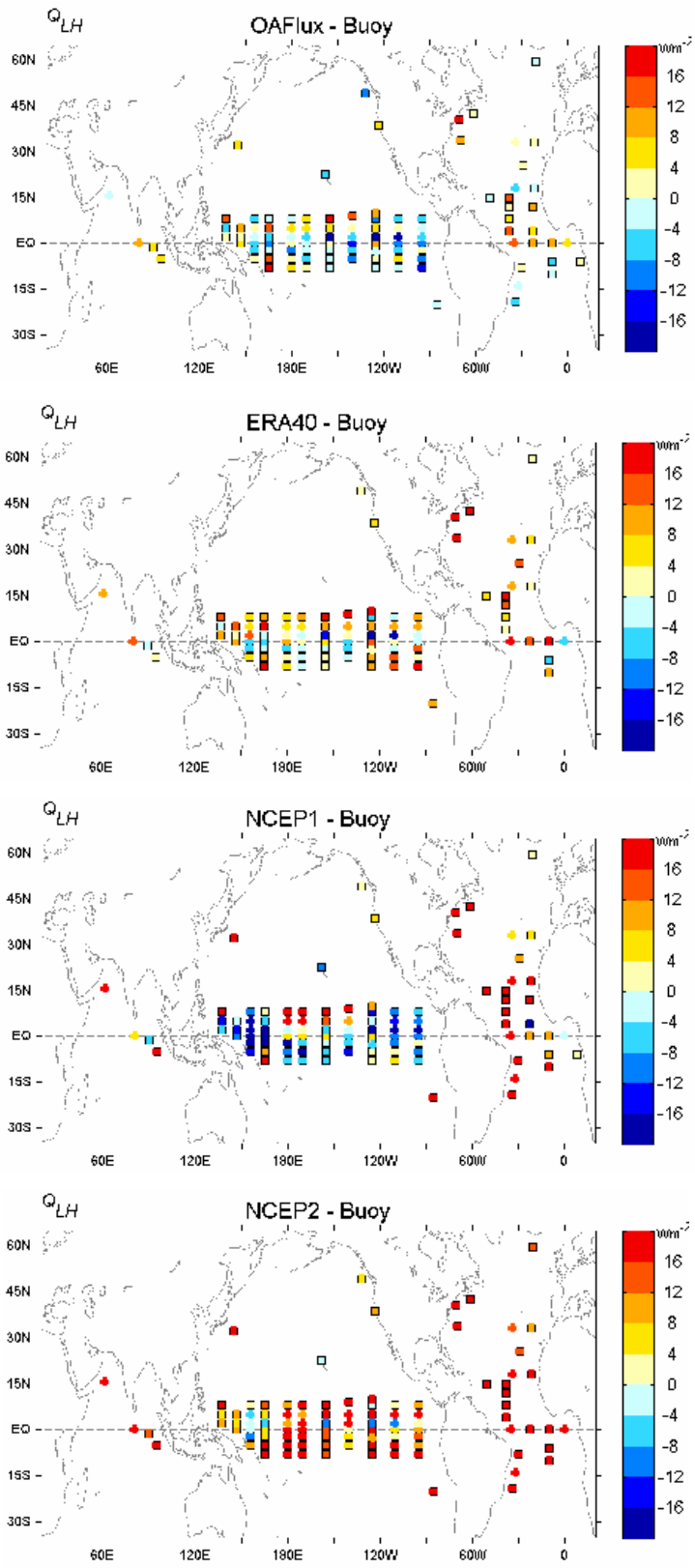

Fig.14 Mean Q_{LH} comparison (product-minus-buoy) at the 105 buoy locations. The mean difference at each location represents the average over the available measurement period.

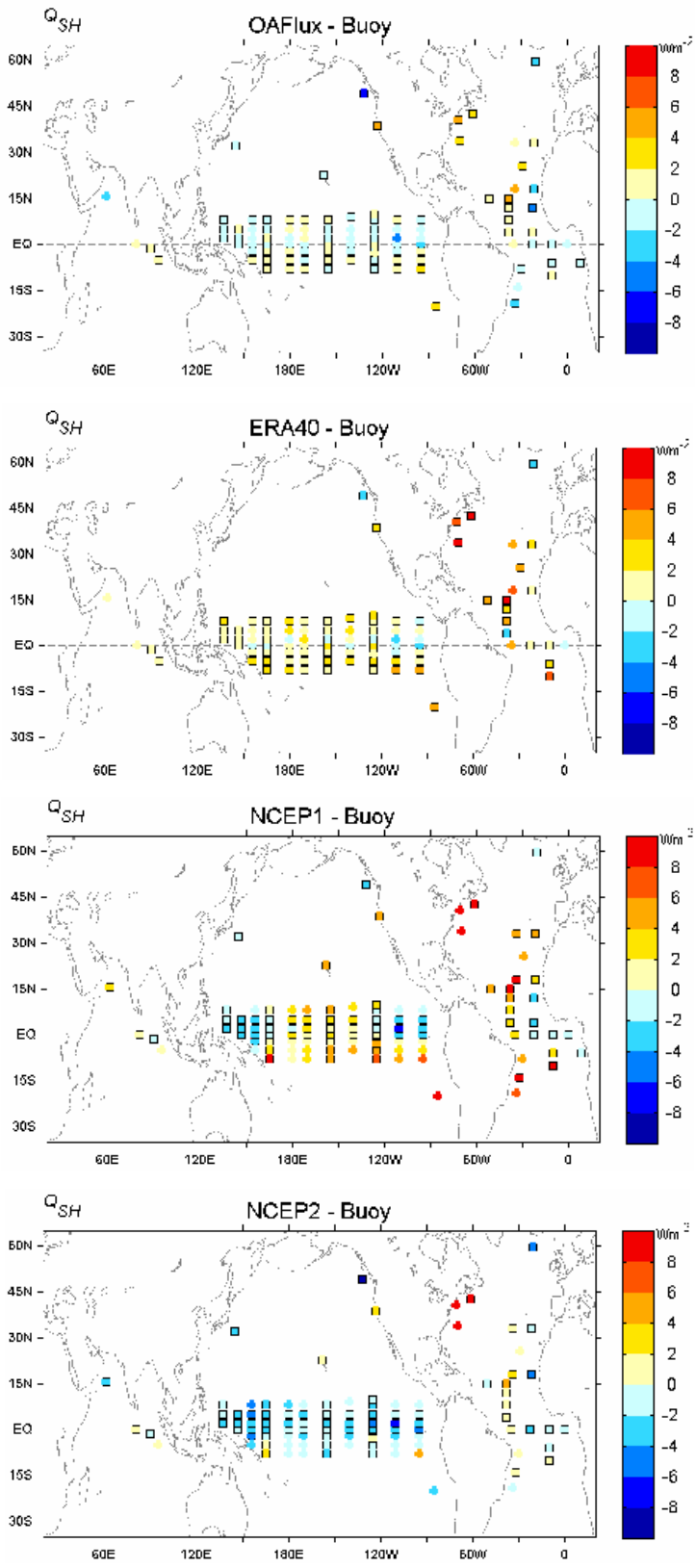

Fig.15 Same as Fig.14 but for Q_{SH}.

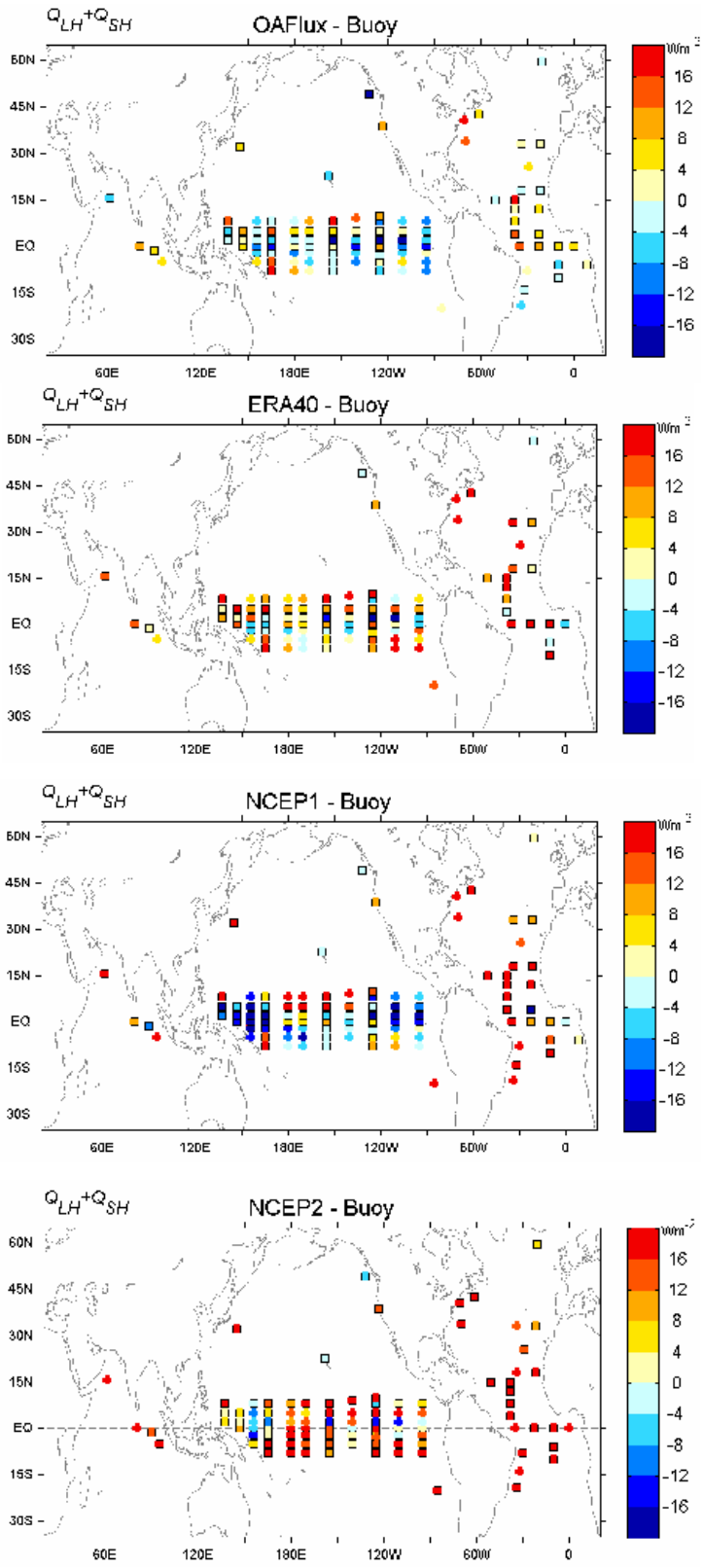

Fig.16 Same as Fig.14 but for Q_{LH}+Q_{SH}.

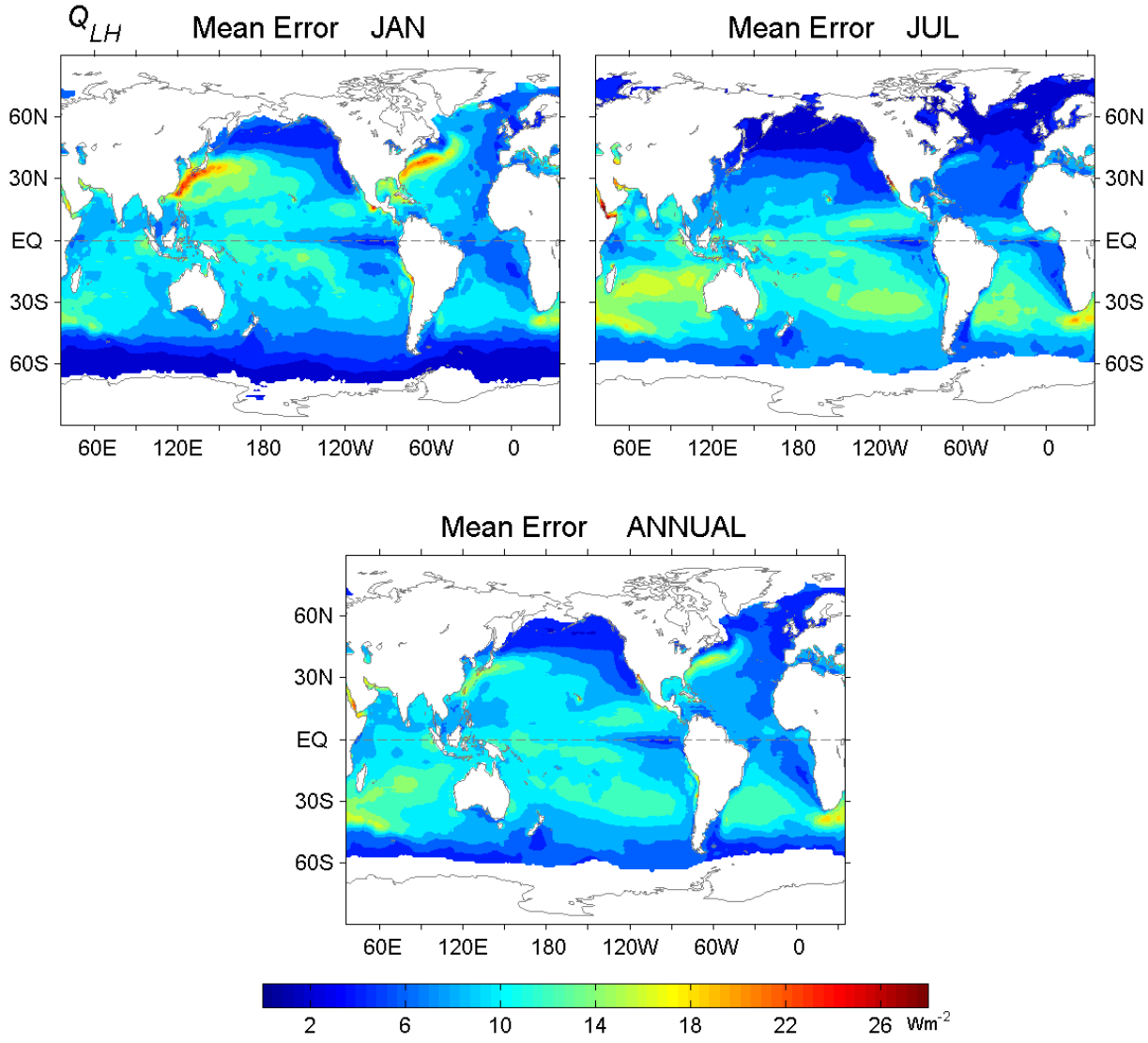

Fig.17 Estimated monthly mean error (standard deviation) for Q_{LH} for (Top right) January, (Top left) July, and (Bottom) annual average. The fields are the average over the 49-year (1958-2006) period.

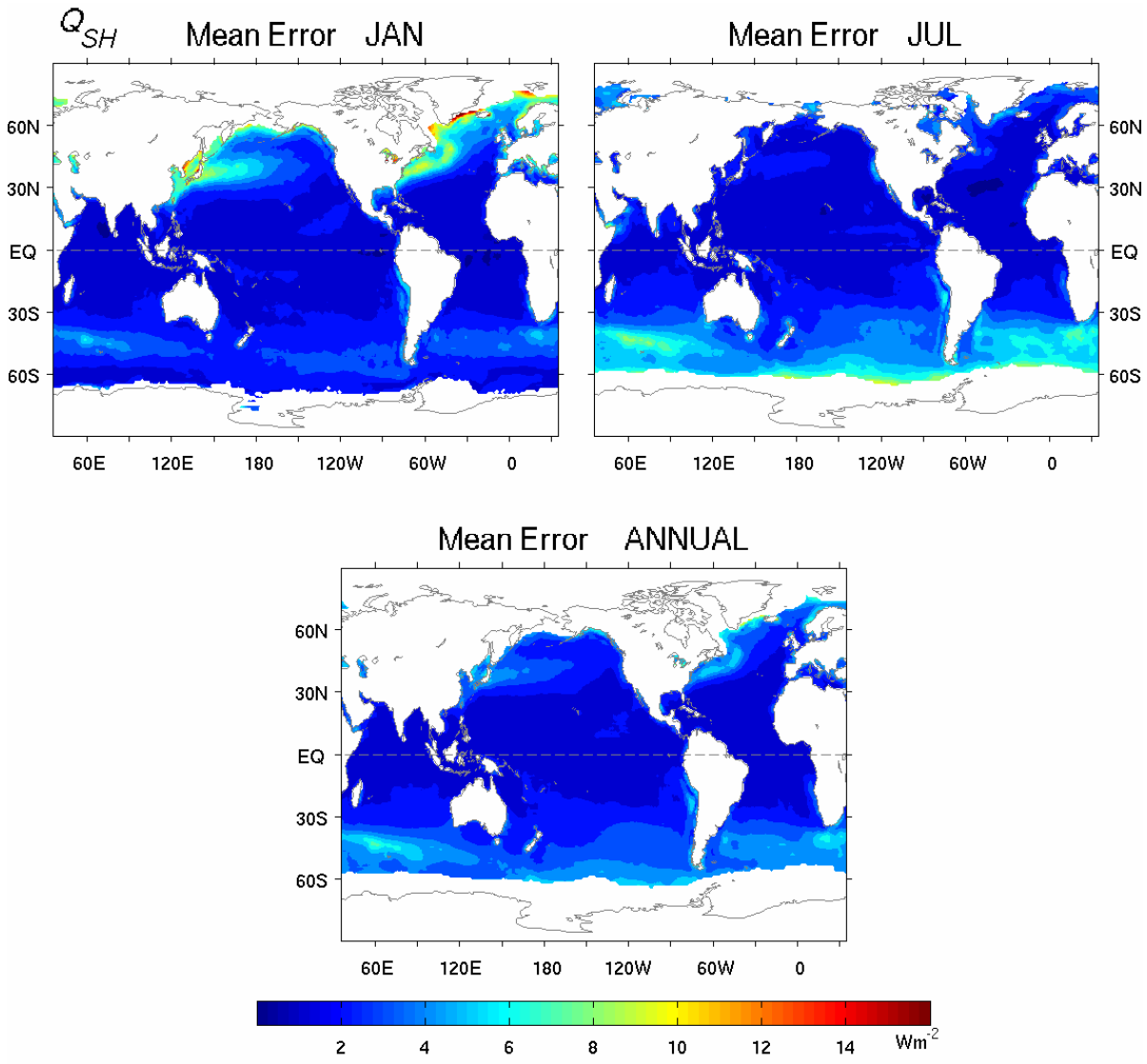

Fig.18 Same as Fig.17 but for Q_{SH}.

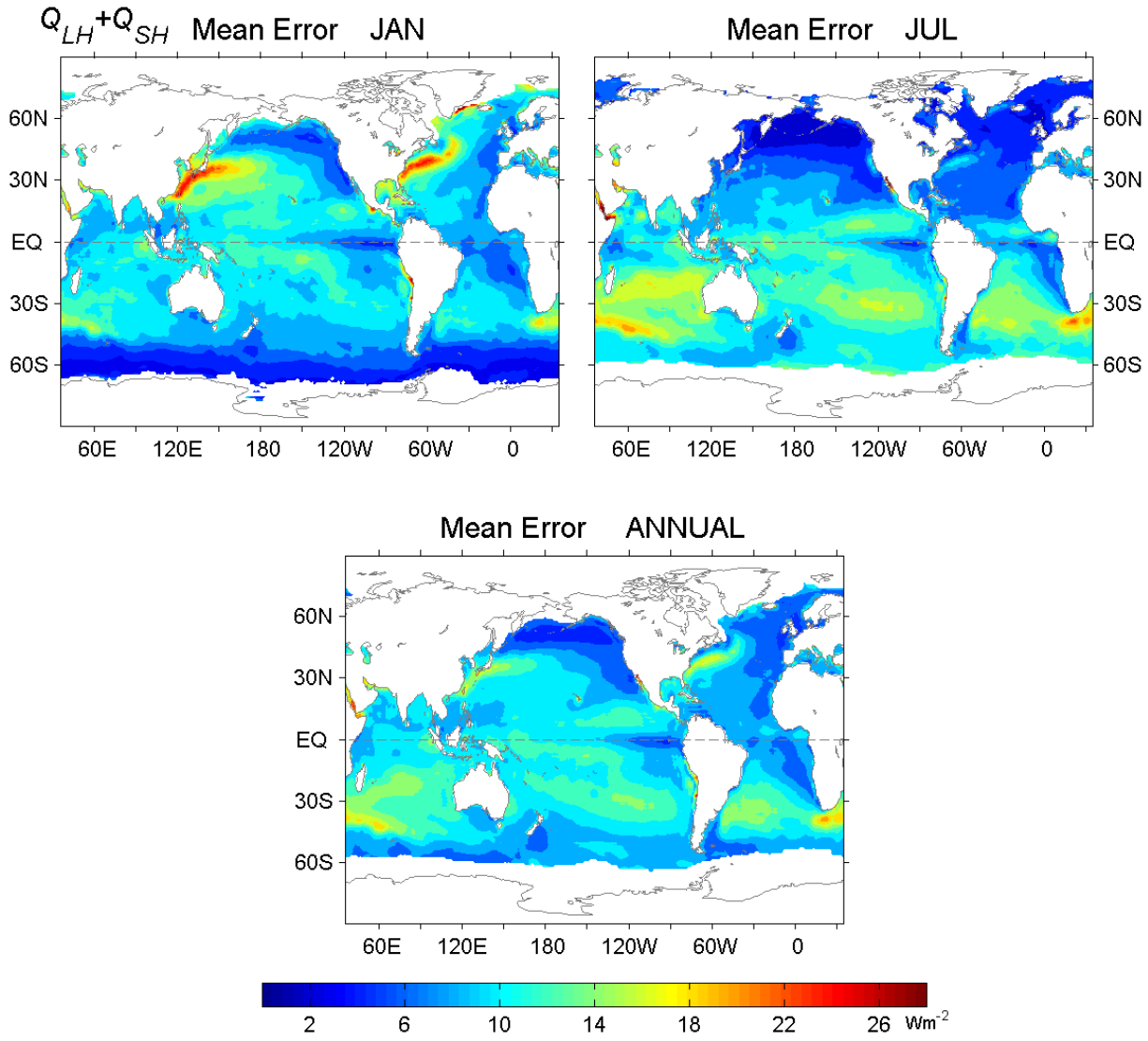

Fig. 19 Same as Fig.17 but for Q_{LH} + Q_{SH}.

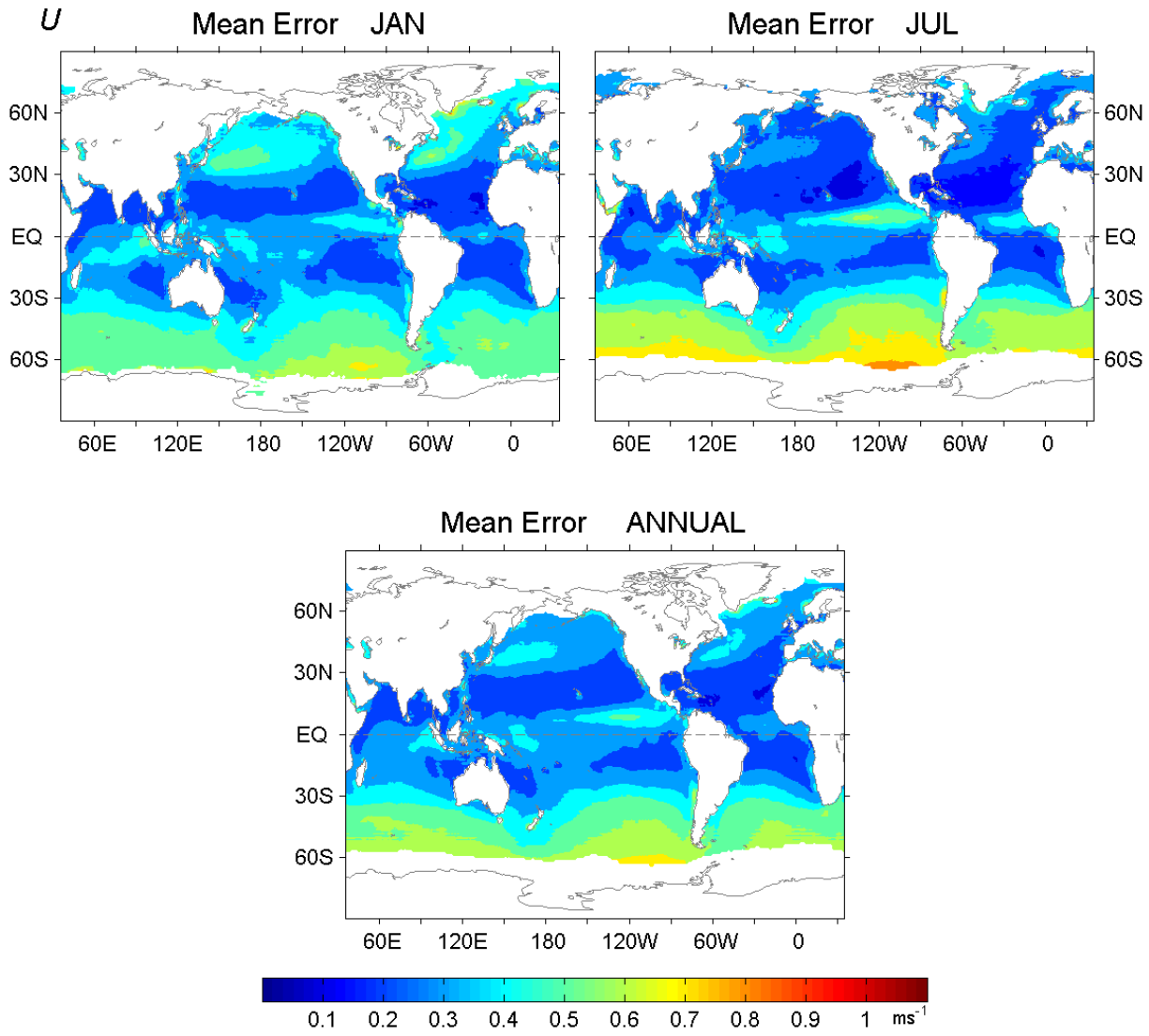

Fig.20 Same as Fig.17 but for *U*.

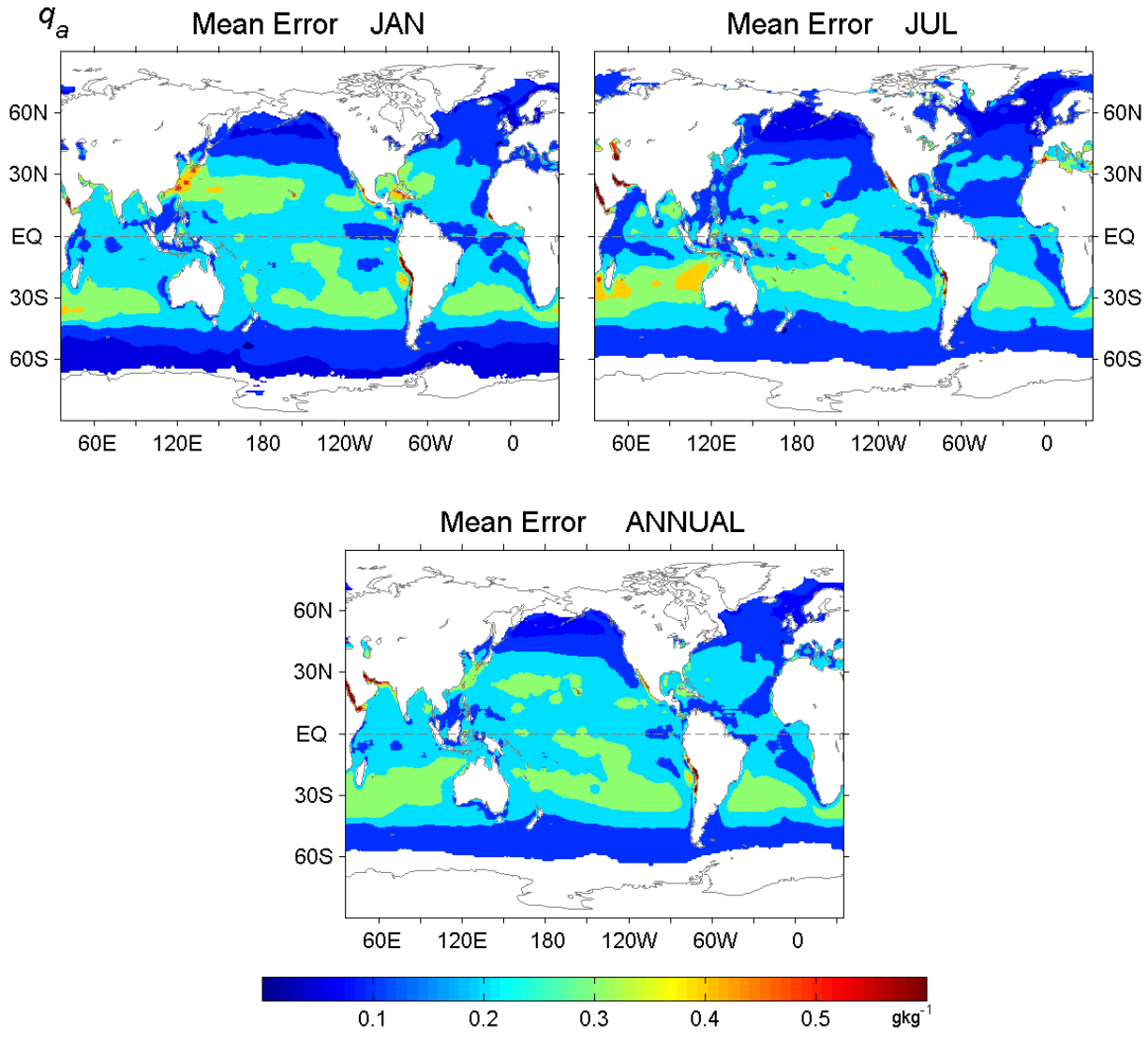

Fig.21 Same as Fig.17 but for q_a.

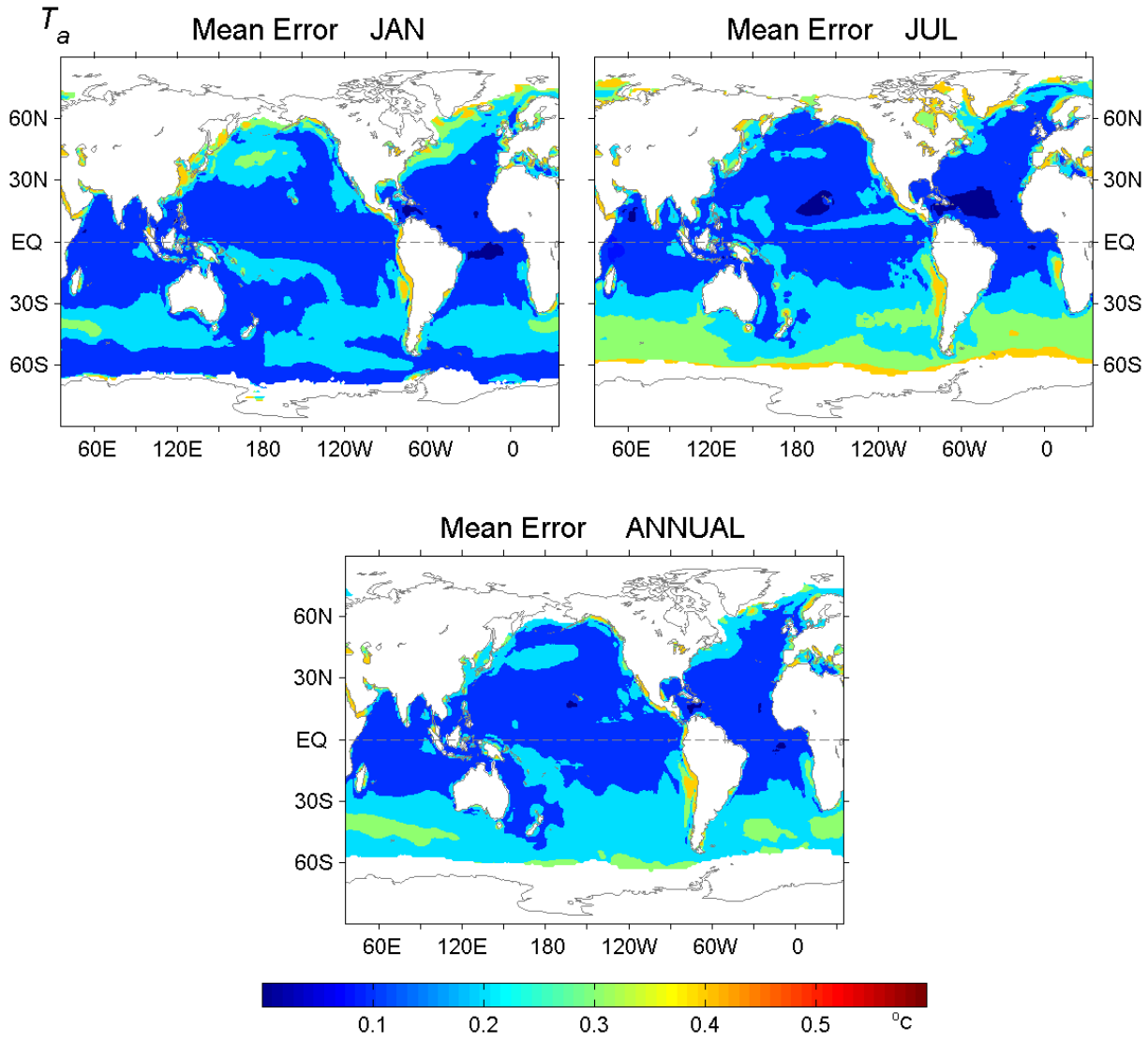

Fig.22 Same as Fig.17 but for T_a.

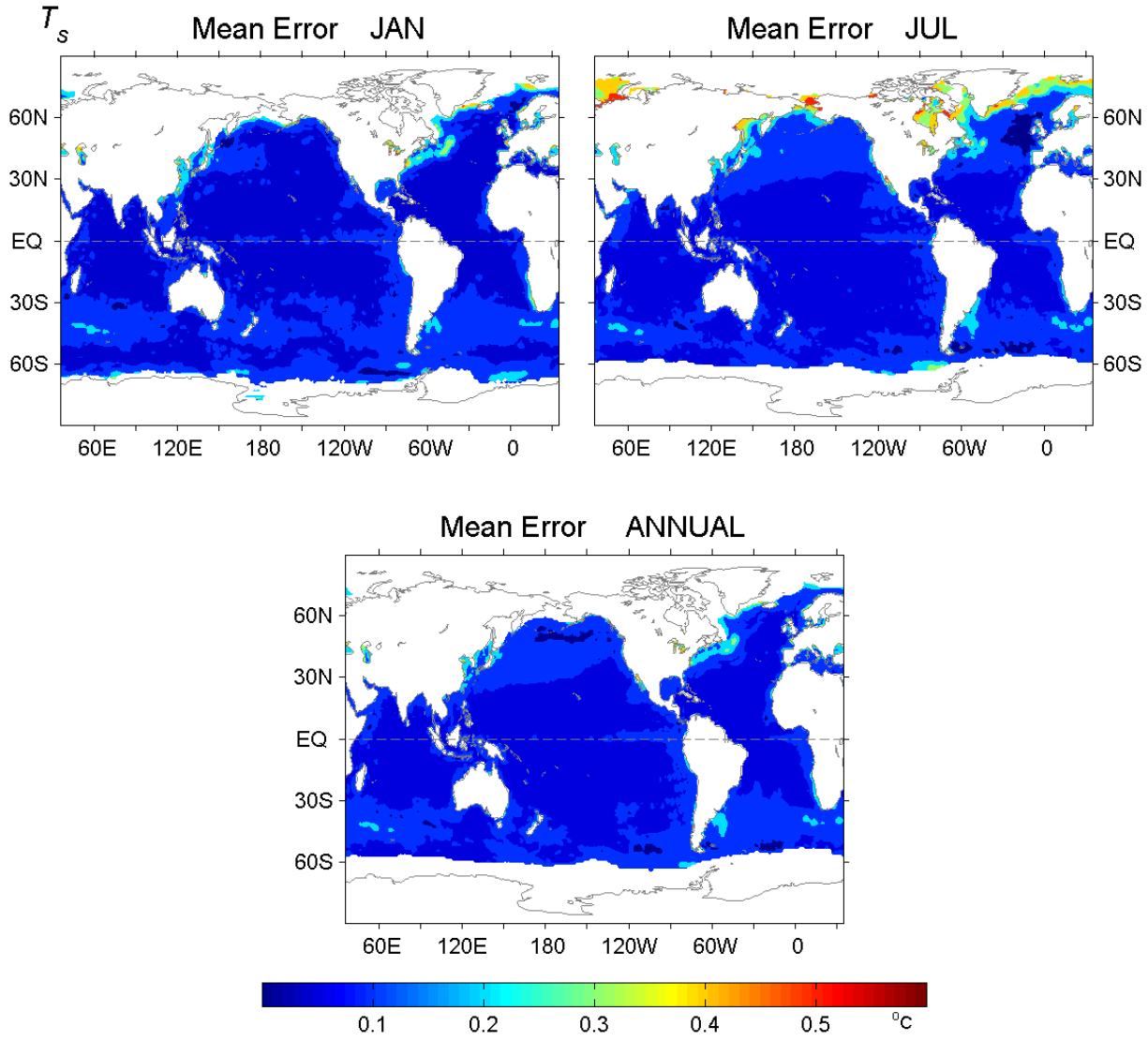

Fig.23 Same as Fig.17 but for T_s.